Hydrodynamical flow and hadron spectra in ultrarelativistic heavy ion collisions at RHIC and the LHC

Harri Niemi

July 16, 2008

Preface

The work reviewed in this thesis has been carried out during the years 2002-2008 at the Department of Physics in the University of Jyväskylä.

This work is a result of many years of work not only by me but also several other people. I am very grateful to all who have helped to make this project easier. Most of all I wish to thank my supervisors Prof. Vesa Ruuskanen and Prof. Kari J. Eskola for introducing me into the fascinating field of ultrarelativistic heavy ion collisions and for continuous and tireless support and guidance during these years. I have had a luxury of having not only one but two excellent supervisors. A considerable part of this work has been done with Dr. Sami Räsänen, whom I wish to thank for pleasant collaboration. I also wish to thank the staff and friends at the Department of Physics for making the Department an excellent place to work. Special thanks go to the ladies in the office, for making all practical matters run smoothly.

Finally, I wish to thank my friends and parents, not for helping me to write this thesis, but for distracting me from it.

Jyväskylä, July 2008

Harri Niemi

List of Publications

This thesis consists of an introductory part and the following publications:

I **Dependence of hadron spectra on decoupling temperature and resonance contributions**,
K. J. Eskola, H. Niemi, P. V. Ruuskanen and S. S. Räsänen,
Phys. Lett. B **566**, 187 (2003), [arXiv:hep-ph/0206230].

II **RHIC-tested predictions for low-p(T) and high-p(T) hadron spectra in nearly central Pb + Pb collisions at the LHC**,
K. J. Eskola, H. Honkanen, H. Niemi, P. V. Ruuskanen and S. S. Räsänen,
Phys. Rev. C **72**, 044904 (2005), [arXiv:hep-ph/0506049].

III **Dynamical freeze-out condition in ultrarelativistic heavy ion collisions**,
K. J. Eskola, H. Niemi and P. V. Ruuskanen,
Phys. Rev. C **77**, 044907 (2008), [arXiv:0710.4476 [hep-ph]].

IV **Elliptic flow in nuclear collisions at the Large Hadron Collider**,
H. Niemi, K. J. Eskola and P. V. Ruuskanen,
arXiv:0806.1116 [hep-ph], submitted to Phys. Rev. C.

The author has developed an independent hydrodynamical code to calculate the hydrodynamical evolution including a finite net-baryon number in papers I and II. He participated also in the planning and writing of these papers.

The author has developed the computer codes used and performed all the numerical calculations for the papers III and IV. The draft versions of the papers III and IV were written by the author.

Contents

Chapter 1

Introduction

One of the main goals of the research of ultrarelativistic heavy ion collisions is to study the thermodynamics of the strongly interacting matter. The fundamental constituents of the strongly interacting matter are quarks and gluons, and the theory describing their interactions is Quantum Chromo-dynamics (QCD). At low density and temperature the degrees of freedom of the QCD matter are hadrons, bound states of quarks and gluons. Currently there are hundreds of known hadronic states [1]. When the density or temperature increases, the transition from the hadronic state to the Quark-Gluon Plasma (QGP), where the degrees of freedom are quarks and gluons, is expected to happen [2].

Theoretically the most direct and rigorous information on the properties of the QCD matter is obtained from numerical lattice simulations of QCD. These simulations indicate that, at low baryon density, the transition from the Hadron Resonance Gas (HRG) to the QGP happens at a temperature $150 - 190$ MeV [3]. Experimentally the properties of matter can be best accessed in ultrarelativistic heavy ion collisions [4]. In these collisions a large number of particles is produced in a small space-time region, giving rise to a large energy density. At high enough collision energies, $\sqrt{s} \gtrsim 20$ GeV, the matter initially produced is expected to be in the form of QGP [5]. This state then cools down and the transition back to the HRG occurs. In contrast to the lattice calculations, which provide information on the static properties of the QCD matter, the system formed in a heavy ion collision is a highly dynamical one. Therefore, a good phenomenological understanding of the dynamics is required in order to extract the properties of the QCD matter from the data provided by the heavy ion experiments.

In a microscopical approach the dynamics of the QCD matter is described directly by calculating individual quark and gluon interactions [6, 7]. Although the high-energy interactions of quarks and gluons, *e.g.* in proton-proton collisions, can be described directly by QCD, using perturbative techniques (pQCD), these methods become unreliable at the thermal energies

which need to be considered in heavy ion collisions. Especially, in the microscopical modeling it is hard to correctly describe the transition from quarks and gluons to the hadronic degrees of freedom when the QGP turns into the HRG as the matter cools down.

A different view to the dynamics is provided by hydrodynamical models [8, 9, 10, 11]. In these models the treatment of the dynamics is not based on individual particle interactions. Instead, the matter is described as a continuous fluid in or close to a local thermal equilibrium, and the dynamical properties of the matter are given by its Equation of State (EoS). The expansion dynamics can then be described in terms of differential equations, which express the local conservation of energy and momentum. The hydrodynamical approach is considerably simpler than the microscopical modeling, and because it is based on the assumption of thermal equilibrium, it is directly connected to the thermodynamical properties of the system. Therefore, it can provide complementary information on the dynamics of the strongly interacting matter.

The key input to the hydrodynamical models, besides the EoS, are the initial energy and net-baryon densities. The initial state cannot be given by the hydrodynamical models themselves, as the initial particle production in nucleus-nucleus collisions is clearly a non-equilibrium process that cannot be treated with an assumption of a thermal equilibrium alone. Therefore the initial state must be obtained from somewhere else. One way to use the hydrodynamical models is to fit the parametrization of the initial state and the other model parameters to the available experimental data, and in this way get constraints on the possible initial state [12, 13]. Another possibility is to use an initial state which is calculated from either the QCD theory or from a model extracted from the known properties of QCD [14, 15]. Once the calculations are made in a closed framework, then also controlled predictions for higher collision energies can be made. This is the approach used here.

The system formed in an ultrarelativistic heavy ion collision is strongly expanding and has a finite size and lifetime. In the experiments at the Relativistic Heavy Ion Collider (RHIC) only O(1000) final state particles are detected in the central rapidity unit. Obviously the system is still not a macroscopic system with O(10^{23}) particles. Therefore it is not clear to what extent the assumption of the local thermal equilibrium holds. However, currently there are several measured low-p_T observables in nucleus-nucleus collisions at RHIC [16, 17, 18, 19], that are consistent with the predictions of the perfect-fluid (nonviscous) hydrodynamical models [20, 21, 22]. In particular, the consistency of the measured elliptic flow with the hydrodynamical calculations has been argued to point to fast thermalization [23] and low viscosity [24] of the matter formed in these collisions. Recently, also dissipative effects have been considered in the hydrodynamical calculations [25, 26, 27, 28, 29, 30, 31, 32]. These results also point towards a low

3

viscosity of the QCD matter.

The heavy ion program at the Large Hadron Collider (LHC) at CERN will provide an even better environment than RHIC to study the detailed properties of the QCD matter. With the larger collision energy, the system produced in Pb + Pb collisions at the LHC is expected to have clearly larger initial energy density and temperature than at RHIC. Therefore, also the lifetime of the QGP phase is expected to be significantly longer. With the larger number of particles and the longer lifetime of the system, also the use of the hydrodynamical models should be better justified at the LHC than at RHIC. Hydrodynamical behavior at the LHC has been discussed in Refs. [II, IV, 33, 34, 35, 36, 37, 38, 39, 40], using different initializations and different estimates for the charged hadron multiplicity, which can be found in Refs. [40, 41].

This thesis consists of four original research papers [I], [II], [III] and [IV], and the introductory and summary part presented below. The hydrodynamical equations and the EoS are presented in Chap. 2. The numerical method which is used for solving the hydrodynamical equations, is introduced in Chap. 3. The Cooper-Frye decoupling procedure, resonance decays and different decoupling conditions are discussed in Chap. 4. The initialization of the hydrodynamical calculations using the EKRT model [14] is briefly summarized in Chap. 5. The main results of this thesis regarding the hydrodynamical evolution, hadron spectra and elliptic flow at RHIC and the LHC are discussed in Chaps. 6 and 7. Finally, conclusions and outlook are given in Chap. 8.

Chapter 2

Hydrodynamical models

In contrast to microscopical models (see *e.g.* Ref. [42]), where the dynamics of a many-particle system is described through the detailed properties of particle interactions, hydrodynamical models describe such a system as a continuous fluid with properties given through a few macroscopic quantities like the EoS and dissipative coefficients for viscosity and heat conductivity. These parameters can in principle be derived from a given microscopical theory of particle interactions. However, in a phenomenological approach the parameters can also be inferred from experimental data. The main advantage of the hydrodynamical model is its simplicity: it is based on the assumption that the system is close to thermodynamical equilibrium, thus particle interactions need not to be explicitly specified. One of the main goals in the heavy ion research is to gain information on the thermodynamical properties of the QCD matter. In thermal equilibrium the properties of the matter are given by its EoS, which is a direct input to the hydrodynamical model. In this sense hydrodynamics is a natural framework to study thermodynamics of a dynamical system.

The basic equations describing the hydrodynamical evolution are the local conservation laws of energy and momentum, together with the conservation laws of additional conserved quantities like the net-baryon number. The state of the matter is given by the energy-momentum tensor $T^{\mu\nu}$, which is a symmetric 4×4 tensor, and the charge currents j_i^μ. In the general case $T^{\mu\nu}$ has 10 and each j_i^μ 4 independent components. Local conservation laws in the covariant form are given by [43]

$$\partial_\mu T^{\mu\nu} = 0, \tag{2.1}$$

$$\partial_\mu j_i^\mu = 0. \tag{2.2}$$

If the conserved charges are restricted to the net-baryon number, we have 5 equations for 14 independent quantities. Obviously the system has to be restricted further in order to get a closed set of equations. One possibility to obtain more insight on the structure of $T^{\mu\nu}$ and j_B^μ is to make a tensor

decomposition with respect to an arbitrary time-like 4-vector u^μ, normalized as $u^2 = 1$. For this purpose we define a projection operator $\Delta^{\mu\nu}$ with the following properties:

$$\Delta^{\mu\nu} = g^{\mu\nu} - u^\mu u^\nu, \ \ \Delta^{\mu\nu} u_\mu = 0, \ \ \Delta^{\mu\alpha} \Delta^\nu_\alpha = \Delta^{\mu\nu}, \tag{2.3}$$

where the metric tensor is given by $g^{\mu\nu} = \text{diag}(1, -1, -1, -1)$. The decomposition of the net-baryon current reads then [44]

$$j^\mu_B = n_B u^\mu + \nu^\mu, \tag{2.4}$$

where

$$n_B = u_\mu j^\mu_B. \tag{2.5}$$

The component orthogonal to u^μ is given by

$$\nu^\mu = \Delta^{\mu\nu} j_{B,\nu}. \tag{2.6}$$

Similarly, the tensor $T^{\mu\nu}$ can be decomposed as

$$T^{\mu\nu} = \epsilon \, u^\mu u^\nu - p \, \Delta^{\mu\nu} + q^\mu u^\nu + q^\nu u^\mu + \pi^{\mu\nu}, \tag{2.7}$$

where

$$\epsilon = u_\mu T^{\mu\nu} u_\nu, \tag{2.8}$$

$$p = -\frac{1}{3} \Delta_{\mu\nu} T^{\mu\nu}, \tag{2.9}$$

$$q^\mu = \Delta^{\mu\alpha} T_{\alpha\beta} u^\beta, \tag{2.10}$$

$$\pi^{\mu\nu} = \left[\frac{1}{2} \left(\Delta^\mu_\alpha \Delta^\nu_\beta + \Delta^\mu_\beta \Delta^\nu_\alpha \right) - \frac{1}{3} \Delta^{\mu\nu} \Delta_{\alpha\beta} \right] T^{\alpha\beta}. \tag{2.11}$$

The physical interpretation of the different terms can be obtained by choosing u^μ to be the fluid 4-velocity. With this choice, two mechanisms for the transport of the energy, momentum and baryon number can be identified: convection, transport parallel to u^μ and diffusion, transport orthogonal to u^μ. The frame where $u^\mu = \gamma(1, \mathbf{v}) = (1, \mathbf{0})$, where γ is the Lorentz gamma factor, is called the local rest frame (LRF). The energy and net-baryon densities in the LRF are given by ε and n_B, respectively. The term ν^μ describes the diffusion of the net-baryon number orthogonal to the fluid velocity. Similarly, q^μ describes the diffusion of energy and $\pi^{\mu\nu}$ the diffusion of momentum. These two terms are related to the heat conductivity and the viscosity of the system. The isotropic momentum transfer rate is given by p. In thermal equilibrium p coincides with the thermodynamical pressure, and it is usually called isotropic pressure even if the system is not in thermal equilibrium.

In a general case the fluid velocity is not unique, but it can be associated with, *e.g.* any conserved charge in the system. For the systems discussed

6

here, the conserved quantities are the net-baryon number, energy and momentum. Different choices lead to different fluid velocities. If u^μ is defined as

$$u^\mu = \frac{j_B^\mu}{\sqrt{j_B \cdot j_B}}, \tag{2.12}$$

the fluid velocity is chosen in the direction of the total flux of the net-baryon number. With this choice there is, by definition, no net baryon flux orthogonal to u^μ and $\nu^\mu = 0$. Another choice would be to choose u^μ in the direction of the energy flux, which would lead to vanishing heat conduction, *i.e.* to $q^\mu = 0$.

In the kinetic theory the energy-momentum tensor can be written as a function of a single-particle momentum distribution function $f(x, p)$ [45]:

$$T^{\mu\nu}(x) = \int \frac{d^3 \mathbf{p}}{p^0} p^\mu p^\nu f(x, p). \tag{2.13}$$

An assumption that greatly simplifies the form of the energy-momentum tensor is that of local thermal equilibrium, *i.e.* $f(x, p)$ is given by the Bose-Einstein or Fermi-Dirac distribution functions:

$$f(p) = \frac{1}{(2\pi)^3} \frac{1}{e^{(p \cdot u - \mu)/T} \pm 1}. \tag{2.14}$$

For this choice the x-dependence in $T^{\mu\nu}$ is through the flow velocity $u^\mu(x)$, the temperature $T(x)$ and the chemical potential $\mu(x)$. Thus the energy-momentum tensor can only be of the form

$$T^{\mu\nu}(x) = A(x)u^\mu(x)u^\nu(x) + B(x)\Delta^{\mu\nu}(x), \tag{2.15}$$

where the coefficients $A(x)$ and $B(x)$ can depend only on scalar quantities. In particular, the energy-momentum tensor does not depend on the gradients of the hydrodynamical variables. Comparing this form with the general decomposition, Eq. (2.7), we see that in local thermal equilibrium $T^{\mu\nu}$ is given by

$$T^{\mu\nu}(x) = [\varepsilon(x) + p(x)] u^\mu(x)u^\nu(x) - p(x)g^{\mu\nu}, \tag{2.16}$$

where ε is the local energy density and p is the pressure given by Eq. (2.9). In thermal equilibrium the kinetic pressure coincides with the thermodynamic pressure and is given by the EoS. With the same assumptions the form of the net-baryon current is

$$j_B^\mu(x) = n_B(x)u^\mu(x), \tag{2.17}$$

where $n_B(x)$ is the local net-baryon density. The theory described by the conservation laws with energy-momentum tensor of the form (2.16) and the

conserved current of the form (2.17) is called perfect-fluid hydrodynamics. From Eq. (2.16) it can be shown that the fluid velocity is given by

$$v^i = \frac{T^{0i}}{T^{00} + p}.$$ (2.18)

Therefore the choice of the flow velocity in the perfect-fluid hydrodynamics is unique. The perfect-fluid hydrodynamics is nondissipative, *i.e.* there is no heat conductivity, viscosity or baryon diffusion. In thermal equilibrium the entropy density s is given by

$$s = \frac{\varepsilon + p - \mu_B n_B}{T},$$ (2.19)

where μ_B is the baryon chemical potential. In nondissipative hydrodynamics there is no entropy production, *i.e.* the entropy is conserved:

$$\partial_\mu(su^\mu) = 0.$$ (2.20)

The conservation law of the entropy is not an additional equation to be solved, but a direct consequence of the assumption of local thermal equilibrium and of the conservation laws (2.1) and (2.2).

In relativistic hydrodynamics the energy density and the net-baryon density are frame dependent. In the perfect-fluid hydrodynamics, the connection between the tensor components $T^{0\mu}$ in an arbitrary frame and the energy density in the LRF is given by

$$\varepsilon = T^{00} - \sum_i \left(T^{0i}\right)^2 \frac{1}{T^{00} + p(\varepsilon, n_B)},$$ (2.21)

and the connection between j_B^0 and n_B is simply

$$n_B = j_B^0/\gamma.$$ (2.22)

Even if the system is not in local thermal equilibrium, but close to it, thermal quantities are still useful. In that case the function $f(x, p)$ can depend also on gradients of hydrodynamical variables (see *e.g.* [44]) and $T^{\mu\nu}$ would not be given by the form (2.16) anymore, but also other terms in the decompositions (2.4) and (2.7) would be nonzero. Thus $T^{\mu\nu}$ would have more independent variables and additional relations would be needed to close the system. This procedure leads to dissipative hydrodynamics, *i.e.* a relativistic generalization of the Navier-Stokes equations [43, 46, 47, 48, 49]. For dissipative hydrodynamics, entropy would be increasing during the evolution, and Eq. (2.20) would not hold, anymore. These equations, however, are not discussed further in this work, but we always assume perfect-fluid hydrodynamics.

Thus, we are left with 5 equations and 6 unknowns. Therefore, an EoS in the form $p = p(\varepsilon, n_B)$ is enough to close the system. Once the initial state is given, the hydrodynamical equations (2.1) and (2.2) can be solved.

2.1 Perfect-fluid hydrodynamics

The conservation laws (2.1) and (2.2) can be written in the perfect-fluid hydrodynamics in Cartesian coordinates as:

$$\partial_t T^{tt} = -\partial_x(\tilde{v}_x T^{tt}) - \partial_y(\tilde{v}_y T^{tt}) - \partial_z(\tilde{v}_z T^{tt}),$$
$$\partial_t T^{tx} = -\partial_x(v_x T^{tx}) - \partial_y(v_y T^{tx}) - \partial_z(v_z T^{tx}) - \partial_x p,$$
$$\partial_t T^{ty} = -\partial_x(v_x T^{ty}) - \partial_y(v_y T^{ty}) - \partial_z(v_z T^{ty}) - \partial_y p, \qquad (2.23)$$
$$\partial_t T^{tz} = -\partial_x(v_x T^{tz}) - \partial_y(v_y T^{tz}) - \partial_z(v_z T^{tz}) - \partial_z p,$$
$$\partial_t j^t = -\partial_x(v_x j^t) - \partial_y(v_y j^t) - \partial_z(v_z j^t),$$

where the velocity $\tilde{v}_i$, appearing in the first equation, is defined as

$$\tilde{v}_i = \frac{T^{ti}}{T^{tt}}. \qquad (2.24)$$

In the other four equations the velocity v_i is given by Eq. (2.18). In ultra-relativistic heavy ion collisions the system forms in a state of a very strong longitudinal expansion. For such systems more convenient coordinates are the light-cone coordinates, defined as

$$\tau = \sqrt{t^2 - z^2}, \qquad (2.25)$$
$$\eta = \frac{1}{2}\ln\left(\frac{t+z}{t-z}\right), \qquad (2.26)$$

where τ is the longitudinal proper time and η is the space-time rapidity. The longitudinal proper time is the time in the coordinate system that starts at $(z = 0, t = 0)$ with a constant velocity v_z and reaches the point z at time t, *i.e.* moves with a velocity $v_z = \frac{z}{t}$. In this coordinate system the conservation laws take the form [50]:

$$\partial_\tau T^{\tau\tau} = -\partial_x(\tilde{v}_x T^{\tau\tau}) - \partial_y(\tilde{v}_y T^{\tau\tau}) - \partial_\eta(\tilde{v}_\eta T^{\tau\tau}) - \frac{1}{\tau}T^{\tau\tau} - \tau v_\eta \tilde{v}_\eta T^{\tau\tau} - \frac{1}{\tau}p,$$

$$\partial_\tau T^{\tau x} = -\partial_x(v_x T^{\tau x}) - \partial_y(v_y T^{\tau x}) - \partial_\eta(v_\eta T^{\tau x}) - \frac{1}{\tau}T^{\tau x} - \partial_x p,$$

$$\partial_\tau T^{\tau y} = -\partial_x(v_x T^{\tau y}) - \partial_y(v_y T^{\tau y}) - \partial_\eta(v_\eta T^{\tau y}) - \frac{1}{\tau}T^{\tau y} - \partial_y p,$$

$$\partial_\tau T^{\tau\eta} = -\partial_x(v_x T^{\tau\eta}) - \partial_y(v_y T^{\tau\eta}) - \partial_\eta(v_\eta T^{\tau\eta}) - \frac{3}{\tau}T^{\tau\eta} - \frac{1}{\tau^2}\partial_\eta p,$$

$$\partial_\tau j^\tau = -\partial_x(v_x j^\tau) - \partial_y(v_y j^\tau) - \partial_\eta(v_\eta j^\tau) - \frac{1}{\tau}j^\tau.$$

$$(2.27)$$

The equations can be further simplified by assuming boost invariance [9] along the z-direction with a longitudinal flow velocity $v_z = z/t$, which corresponds to $v_\eta = 0$. With this choice, all hydrodynamical variables become

independent of η and the conservation laws are [23]:

$$\partial_\tau T^{\tau\tau} = -\partial_x(\tilde{v}_x T^{\tau\tau}) - \partial_y(\tilde{v}_y T^{\tau\tau}) - \frac{1}{\tau}(T^{\tau\tau} + p),$$

$$\partial_\tau T^{\tau x} = -\partial_x(v_x T^{\tau x}) - \partial_y(v_y T^{\tau x}) - \frac{1}{\tau}T^{\tau x} - \partial_x p,$$

$$\partial_\tau T^{\tau y} = -\partial_x(v_x T^{\tau y}) - \partial_y(v_y T^{\tau y}) - \frac{1}{\tau}T^{\tau y} - \partial_y p, \qquad (2.28)$$

$$\partial_\tau j^\tau = -\partial_x(v_x j^\tau) - \partial_y(v_y j^\tau) - \frac{1}{\tau}j^\tau.$$

In this approximation the original (3+1)-dimensional problem reduces to a (2+1)-dimensional one. A drawback of the simplification is that the model cannot work very far from $\eta \sim 0$, *i.e.* in the region where contributions from the longitudinal boundary of the system are expected to be significant. Formally the approximation of boost invariance corresponds to an infinite-energy collision, where the system is produced at $(t, z) = (0, 0)$ and longitudinal flow velocity approaches the speed of light when the light-cone is approached. Obviously this cannot be exactly true in a realistic heavy ion collision, but can be considered to be a good approximation near $\eta \sim 0$ in nuclear collisions at RHIC and the LHC [51, 52].

Central (impact parameter $b = 0$) collisions are symmetric w.r.t. the azimuthal angle ϕ. For these collisions, it is convenient to write the hydrodynamic equations in cylindrical coordinates

$$x = r\cos\phi, \qquad (2.29)$$

$$y = r\sin\phi. \qquad (2.30)$$

In the symmetric case, the equations become independent of ϕ, and the conservation laws can be written in the following (1+1)-dimensional form [53, 54]:

$$\partial_\tau T^{\tau\tau} = -\partial_r(\tilde{v}_r T^{\tau\tau}) - \frac{1}{r}T^{\tau r} - \frac{1}{\tau}(T^{\tau\tau} + p),$$

$$\partial_\tau T^{\tau r} = -\partial_r(v_r T^{\tau r}) - \frac{1}{r}T^{\tau r} - \frac{1}{\tau}T^{\tau r} - \partial_r p, \qquad (2.31)$$

$$\partial_\tau j^\tau = -\partial_r(v_r j^\tau) - \frac{1}{r}j^\tau - \frac{1}{\tau}j^\tau.$$

The hydrodynamical models we consider in this work are given by Eqs. (2.28) and (2.31). As mentioned above, to close the system of equations, an EoS has to be given.

2.2 Equation of State

In the perfect-fluid hydrodynamics all microscopic properties of the matter are embedded into the EoS. At low temperatures, the QCD excitations are

hadrons and at high temperatures quarks and gluons. The transition temperature T_c from Hadron Resonance Gas (HRG) to Quark-Gluon Plasma (QGP) is obtained from the lattice-QCD calculations and is in the range $T_c \sim 150 - 190$ MeV at $\mu_B = 0$ [3]. In this work a phenomenological EoS [12], described below, is used.

2.2.1 Thermodynamics

In statistical physics all thermodynamical quantities are derived from the partition function. A convenient framework for this is the grand canonical ensemble, where the external restrictions are given by the temperature T, volume V and chemical potential μ. The grand canonical partition function $\mathcal{Z}_G$ is defined as

$$\mathcal{Z}_G = \sum_{\{Nr\}} \exp \beta(\mu N - E_{Nr}), \tag{2.32}$$

where $\beta = 1/T$. The sum is taken over all possible microstates $\{Nr\}$ of the system, where N is the number of particles in the microstate r and E_{Nr} is the energy of the microstate. The partition function gives the probability $p_{\{Nr\}}$ of the microstate when temperature, volume and chemical potentials are fixed,

$$p_{\{Nr\}} = \frac{1}{\mathcal{Z}_G} \exp\left[\beta(\mu N - E_{Nr})\right]. \tag{2.33}$$

The grand canonical potential is defined as

$$\Omega_G(T, V, \mu) = -T \ln \mathcal{Z}_G. \tag{2.34}$$

All thermodynamic quantities can be calculated once $\Omega_G(T, V, \mu)$ or $\mathcal{Z}_G$ is known. From the thermodynamical identities one obtains

$$\Omega_G(T, V, \mu) = -pV, \tag{2.35}$$

i.e. if the pressure of the system is known as a function of T, V and μ, the complete thermodynamics of the system is known.

With the generalization to several chemical potentials, entropy density s, pressure p and particle densities n_i can be obtained by partial differentiation of the partition function:

$$s = \frac{1}{V} \frac{\partial T \ln \mathcal{Z}_G}{\partial T}, \tag{2.36}$$

$$p = T \frac{\partial \ln \mathcal{Z}_G}{\partial V}, \tag{2.37}$$

$$n_i = \frac{T}{V} \frac{\partial \ln \mathcal{Z}_G}{\partial \mu_i}. \tag{2.38}$$

Another useful identity is

$$s = \frac{\varepsilon + p - \sum_i \mu_i n_i}{T}, \tag{2.39}$$

11

where ε is the energy density.

For a mixture of noninteracting particles the logarithm of the partition function can be written as a sum of logarithms of the single-particle partition functions:

$$\ln \mathcal{Z}_G = \sum_i \ln \mathcal{Z}_i, \tag{2.40}$$

where $\mathcal{Z}_i$ is the partition function of particle type i. For noninteracting fermions and bosons the logarithm of the single-particle partition function can be calculated from the definition (2.32), by replacing the sum with an integral, $\sum_{Nr} \rightarrow \sum_N \int \frac{d^3\mathbf{p}}{(2\pi)^3}$. This gives the well-known result

$$\ln \mathcal{Z}_i = \frac{g_i V}{T} \int \frac{d^3\mathbf{p}}{(2\pi)^3} \frac{1}{e^{\beta(E_i - \mu_i)} \pm 1}, \tag{2.41}$$

where g_i is the degeneracy factor and μ_i the chemical potential of the particle. The energy of the particle is $E_i = \sqrt{\mathbf{p}^2 + m_i^2}$, when the interactions between the particles can be neglected. The plus sign is for fermions and the minus sign for bosons. From the above results we obtain:

$$p(T, \{\mu_i\}) = \sum_i g_i \int \frac{d^3\mathbf{p}}{(2\pi)^3} \frac{p^2}{3E_i} \frac{1}{e^{\beta(E_i - \mu_i)} \pm 1}, \tag{2.42}$$

$$n(T, \{\mu_i\}) = \sum_i g_i \int \frac{d^3\mathbf{p}}{(2\pi)^3} \frac{1}{e^{\beta(E_i - \mu_i)} \pm 1}, \tag{2.43}$$

$$\varepsilon(T, \{\mu_i\}) = \sum_i g_i \int \frac{d^3\mathbf{p}}{(2\pi)^3} \frac{E_i}{e^{\beta(E_i - \mu_i)} \pm 1}, \tag{2.44}$$

where the sums are over all particle species included in the EoS.

In this work, we consider two charges, net-baryon number and strangeness, which both are conserved in strong interactions. Strangeness is not conserved in weak interactions, but since the lifetimes of the systems formed in heavy ion collisions are short compared with typical weak-interaction reaction times, strangeness can also be taken as a conserved charge. Since both charges are now conserved in particle reactions, the chemical potential of particle i can be written as

$$\mu_i = B_i \mu_B + S_i \mu_S, \tag{2.45}$$

where B_i is the baryon number and S_i the strangeness of the particle i. Because the strangeness of colliding nuclei is zero and there is not enough time to create strangeness through weak interactions during the evolution, the net-strangeness can be assumed to be zero during the whole evolution. The strangeness chemical potential is obtained by requiring net-strangeness to be zero also locally, *i.e.* the net-strangeness density $n_S = 0$. Due to this

condition μ_S becomes a function of T and μ_B and is not an independent variable anymore. The net-baryon density can be written as a function of T and chemical potentials as

$$n_B(T, \{\mu_i\}) = \sum_i B_i g_i \int \frac{d^3\mathbf{p}}{(2\pi)^3} \frac{1}{e^{\beta(E-\mu_i)} \pm 1}, \qquad (2.46)$$

where the sum is over all particle species and μ_i is given by Eq. (2.45).

For massless particles the integrals (2.42), (2.44) and (2.46) can be carried out analytically, with the results

$$p_q + p_{\bar{q}} = g_q \left(\frac{7\pi^2}{360} T^4 + \frac{1}{12} \mu_q^2 T^2 + \frac{1}{24\pi^2} \mu_q^4 \right),$$

$$p_g = g_g \frac{\pi^2}{90} T^4,$$

$$\varepsilon = 3 \sum_{q,\bar{q}} (p_q + p_{\bar{q}}) + 3p_g, \qquad (2.47)$$

$$n_B = \sum_q \left(\frac{1}{3} \mu_q T^2 + \frac{1}{3\pi^2} \mu_q^3 \right),$$

where the subscript q stands for quarks (fermions) and g for gluons (bosons). The chemical potential of u and d quarks is

$$\mu_{u,d} = \frac{1}{3} \mu_B, \qquad (2.48)$$

and the chemical potential of the s quark is zero, because of the strangeness neutrality.

The QGP phase is described by a simple Bag model [55]

$$p = p_{th} - B, \qquad (2.49)$$
$$\varepsilon = \varepsilon_{th} + B, \qquad (2.50)$$

where the Bag constant B describes the vacuum energy density and p_{th} and ε_{th} are given by Eqs. (2.47). The Bag constant makes sure that the QGP phase is the stable phase at high temperatures. Adding all degrees of freedom, *i.e.* 8 colors for gluons and 3 colors and N_f flavors of quarks, with 2 spin states for each particle, the EoS for the QGP can be written as

$$p = \frac{(32 + 21N_f)\pi^2}{180} T^4 + \frac{1}{9} \mu_B^2 T^2 + \frac{1}{192\pi^2} \mu_B^4 - B, \qquad (2.51)$$

$$\varepsilon = 3p + 4B, \qquad (2.52)$$

$$n_B = \frac{2}{9} \mu_B T^2 + \frac{2}{81\pi^2} \mu_B^3. \qquad (2.53)$$

13

For massive particles the integrals (2.42), (2.44) and (2.46) cannot be carried out analytically, but if $\mu_i < m_i$ they can be written as a series of Bessel functions. For a hadron resonance gas (HRG) this gives

$$p = \sum_i \frac{g_i}{2\pi^2} m_i^2 T^2 \sum_{n=1}^{\infty} \frac{(\mp 1)^{n+1}}{n^2} e^{n\mu_i/T} K_2(n\frac{m_i}{T}), \qquad (2.54)$$

$$\varepsilon = 3p + \sum_i \frac{g_i}{2\pi^2} m_i^3 T \sum_{n=1}^{\infty} \frac{(\mp 1)^{n+1}}{n} e^{n\mu_i/T} K_1(n\frac{m_i}{T}), \qquad (2.55)$$

$$n_B = \sum_i \frac{B_i g_i}{2\pi^2} m_i^2 T \sum_{n=1}^{\infty} \frac{(\mp 1)^{n+1}}{n} e^{n\mu_i/T} K_2(n\frac{m_i}{T}), \qquad (2.56)$$

where the sums are over all hadronic states included in the EoS. The minus sign is for fermions and the plus sign for bosons. Numerically these series are a much faster way to calculate the integrals than the direct numerical integration.

The natural variables in hydrodynamics are the energy density and the net-baryon density rather than the temperature and the chemical potentials. Therefore a convenient form of the EoS is given by

$$\begin{aligned}
p &= p\,(\varepsilon, n_B), \\
T &= T(\varepsilon, n_B), \\
\mu_B &= \mu_B(\varepsilon, n_B), \\
\mu_S &= \mu_S(\varepsilon, n_B).
\end{aligned} \qquad (2.57)$$

To obtain this form of the EoS, the expressions (2.51)-(2.56) need to be inverted numerically.

2.2.2   Hadron resonance gas

The equation of state for the HRG as a function of ε and n_B is obtained by solving numerically T, μ_B and μ_S from the following group of equations

$$\begin{aligned}
\varepsilon &= \varepsilon(T, \mu_B, \mu_S), \\
n_B &= n_B(T, \mu_B, \mu_S), \\
n_S &= n_S(T, \mu_B, \mu_S) = 0,
\end{aligned} \qquad (2.58)$$

where ε is given by Eq. (2.55) and n_B by Eq. (2.56). The strangeness density is calculated in the same way as n_B, but replacing the baryon number B_i with the strangeness S_i of the particle. The HRG considered here and in the papers [I, II, III, IV] includes all hadronic states listed by the Particle Data Group [56] up to the mass 2 GeV. Although the HRG is described as a noninteracting gas of hadrons, the main part of attractive interactions can be thought to be taken into account by the inclusion, in addition to
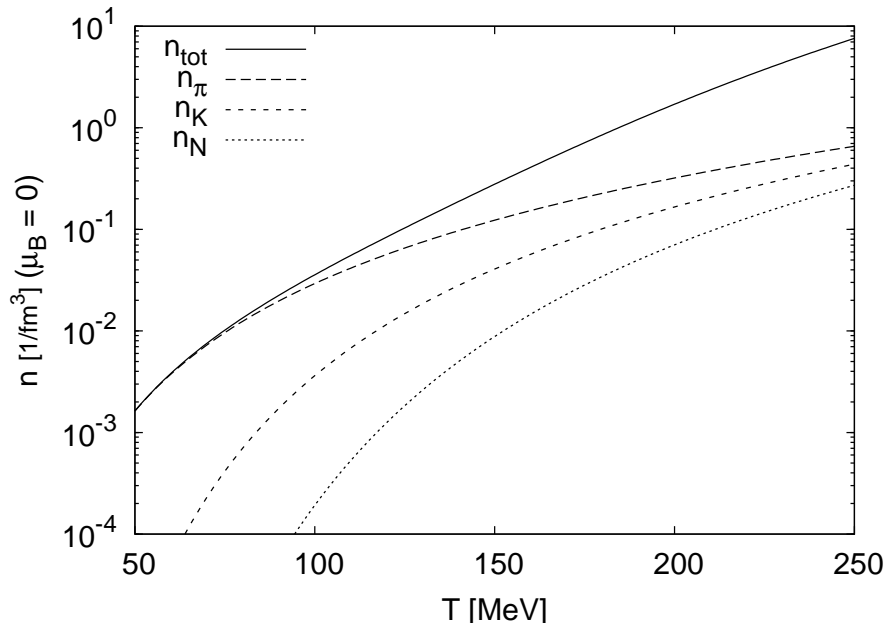
14

Figure 2.1: The number density of pions ($\pi^\pm$, π^0), kaons ($K^\pm$, K^0, $\overline{K}^0$), nucleons (p, $\bar{p}$, n, $\bar{n}$) and of all hadrons in the HRG as a function of temperature. The HRG here includes all hadronic states with $m < 2$ GeV.

the stable hadrons, also of all short-living hadronic resonance states. In Ref. [57] it has been shown that the pressure and the energy density of the interacting pion gas can be well described by the noninteracting pion plus ρ meson gas. Also the lattice QCD results below the critical temperature can be interpreted in terms of a hadron resonance gas [58]. Based on this, hadron plus hadron resonance gas can be thought to give a simple description of the strongly interacting gas of stable hadrons, where stable hadrons include weakly decaying hadrons.

The number of hadronic states increases rapidly with increasing mass: there are only 20 hadronic states up to protons and neutrons ($m \sim 940$ MeV), but the total number of hadronic states, with mass ≤ 2 GeV, included into the HRG is over 300. The density of hadrons is strongly increasing with increasing temperature, as can be seen in Fig. 2.1, which shows the pion, kaon and nucleon density together with the total hadron density as a function of temperature. The density of heavier particles increases faster than that of pions. Therefore the relative contribution from the heavy states increases strongly with temperature. The relative abundances of pions kaons and nucleons are plotted in Fig. 2.2. At the temperatures $T \lesssim 140$ MeV the lightest hadron, the pion, is clearly the dominant component, but as the temperature increases the heavier states become more important. In contrast to the pions, none of the heavier hadrons ever become clearly dominant.
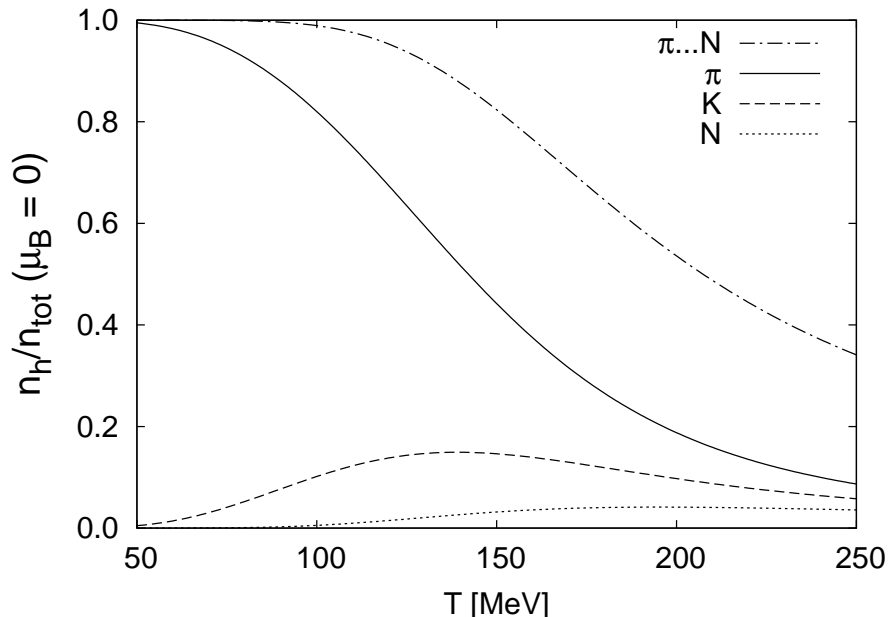
Figure 2.2: Relative abundance of pions, kaons and nucleons in the HRG as a function of temperature. The uppermost curve shows the relative abundance of all hadrons with mass less than or equal to the nucleon mass.

Even the second lightest hadrons, the kaons, contribute at most $\sim 15\%$ and nucleons never more than $\sim 4\%$ to the total density. Figure 2.2 also shows the total number density of hadron states from pions to nucleons relative to the density of all hadrons. These hadrons dominate the HRG up to a temperature $T \sim 200$ MeV, but at temperatures $\gtrsim 150$ MeV the heavier states do still have a significant contribution to the total hadron density.

Another illustrative quantity is the number of hadrons per unit entropy. Since the entropy is conserved in the perfect-fluid hydrodynamics, a constant n_h/s would indicate a conserved number of hadrons for the hadron species h. Figure 2.3 shows these ratios for different hadrons in the HRG. Hydrodynamical evolution in heavy ion collisions starts from high temperatures and during the evolution the matter expands and temperature drops. Changes in the ratios indicate that to keep the system in thermodynamical equilibrium, there must be fast enough particle-number-changing reactions. From the figure we can see that the equilibrium number of light particles, pions and kaons, increases during the evolution, while *e.g.* the number of nucleons decreases below $T \sim 200$ MeV. The total number of hadrons heavier than the nucleons decreases even faster. Thus, in this construction heavy particles annihilate and decay during the evolution and the energy from the heavy states is fed down to the light hadrons, pions and kaons. The number of kaons starts to drop and pions begin to dominate the density of the HRG
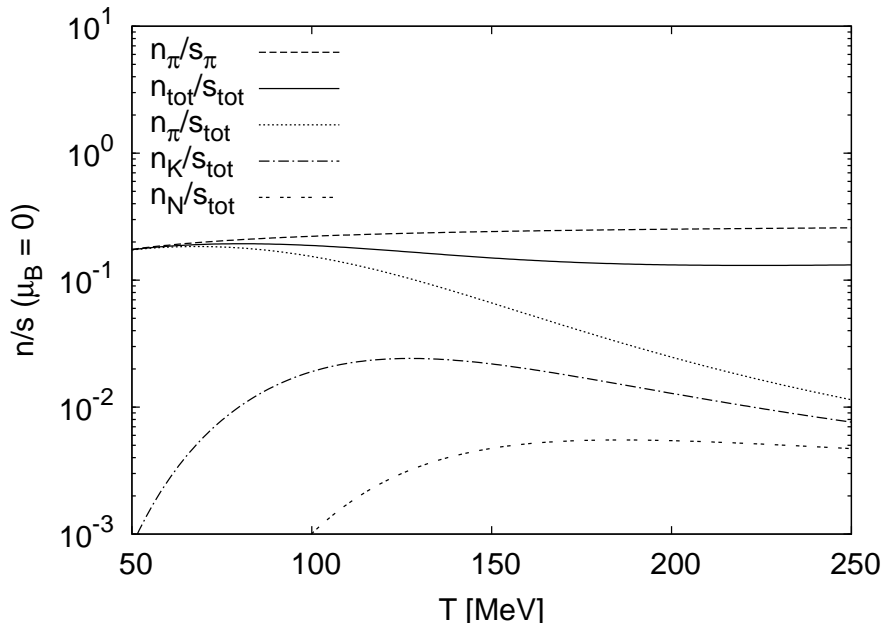
16

Figure 2.3: Number of particles per unit entropy n/s in the HRG as a function of temperature. Also n/s for pions in the HRG and pion gas are shown.

at $T \sim 140$ MeV. Eventually at very low temperatures also the number of pions starts to drop due to the pion mass. The total number of hadrons is more insensitive to the temperature, but it is nevertheless changing by ~ 50 % from $T \sim 200$ MeV to $T \sim 100$ MeV. In the construction of the HRG, full kinetic and chemical equilibrium was assumed, *i.e.* the only conserved charges were the baryon and strangeness numbers. The changes in the chemical composition of the HRG described above are specific to the choice of particle states included in the HRG and to the assumption of full kinetic and chemical equilibrium. For example in the expanding gas consisting only of pions, the number of pions is decreasing at all temperatures, as can be seen from the uppermost curve in Fig. 2.3.

The hadronic system formed in heavy ion collisions has both a finite size and a finite lifetime, and many hadronic reactions have time scales comparable to the lifetime of the system. It is not at all clear that the reactions can maintain thermodynamic equilibrium in the finite, rapidly expanding system. There are several reasons why non-equilibrium effects can be considered to be important. Obviously the hydrodynamical evolution has to end eventually when the system becomes so dilute that its hadrons cannot interact anymore. Typically, in the hydrodynamical models, this break-up happens when $T = 100 - 150$ MeV. Since the cross-sections for particle-number changing reactions are typically smaller than the cross-sections for the elastic scatterings, the chemical composition of the HRG is expected

17

to freeze even before the hydrodynamical evolution ends [59, 60]. Also the interaction rates are different for different types of hadrons, and correspondingly the deviations from equilibrium can be expected to be different for each hadron type. A detailed treatment of the reactions in the HRG would require an EoS that depends not only on the temperature and baryon number, but also on the off-equilibrium chemical abundances of different hadrons. The EoS should then be solved simultaneously with the hydrodynamical equations. An EoS with the separate chemical and kinetic freeze-outs has been used in Refs. [61, 62, 63]. The chemical reactions in the HRG, within the hydrodynamical framework have been studied in Ref. [64]. However, the EoS does not depend dynamically on the chemical composition of the HRG in that work.

The final decoupling of the thermal system to free hadrons clearly involves non-equilibrium processes, and thus it cannot be consistently treated within the equilibrium framework. Typically, the freeze-out is modelled as an instantaneous transition from a thermal system to free hadrons, such that the hadrons maintain their momentum distributions which they had just before the transition. Fully microscopic treatment of the HRG dynamics, such as in the hydro + hadron cascade models [65, 66, 67, 68, 69], have the advantage that the freeze-out can be modelled consistently. These models are, however, much more complex than the thermal treatment presented here, and require a detailed knowledge of the hadronic reactions, many of which are poorly known. Also, at the moment, these models include only 2-particle scatterings. From Fig. 2.1 we see that the density of the HRG is ~ 1 fm^{-3} at $T \sim 200$ MeV, and at such high densities the hadrons are already overlapping with each other, and multiparticle interactions become significant. The maximum density of the HRG depends, obviously, on the transition temperature to the QGP. Especially if this temperature is very high, thermal modelling will be useful as a complementary tool for the HRG dynamics, even if the microscopical models are available. Thermal models give also the full-equilibrium baseline results, with which the effects of different non-equilibrium processes can be compared.

2.2.3   QCD Equation of state

A complete EoS for the strongly interacting matter is obtained here by combining the HRG EoS, given by Eqs. (2.58), and the QGP EoS, given by Eqs. (2.51), (2.52) and (2.53), by using the Maxwell construction. From Eq. (2.35) one sees that a thermodynamical equilibrium state is the one with the highest pressure. Coexistence of two different phases at the temperature T and the chemical potential μ_B requires the pressures in both phases to be the same,

$$p_{\mathrm{HRG}}(T_c, \mu_B) = p_{\mathrm{QGP}}(T_c, \mu_B). \tag{2.59}$$
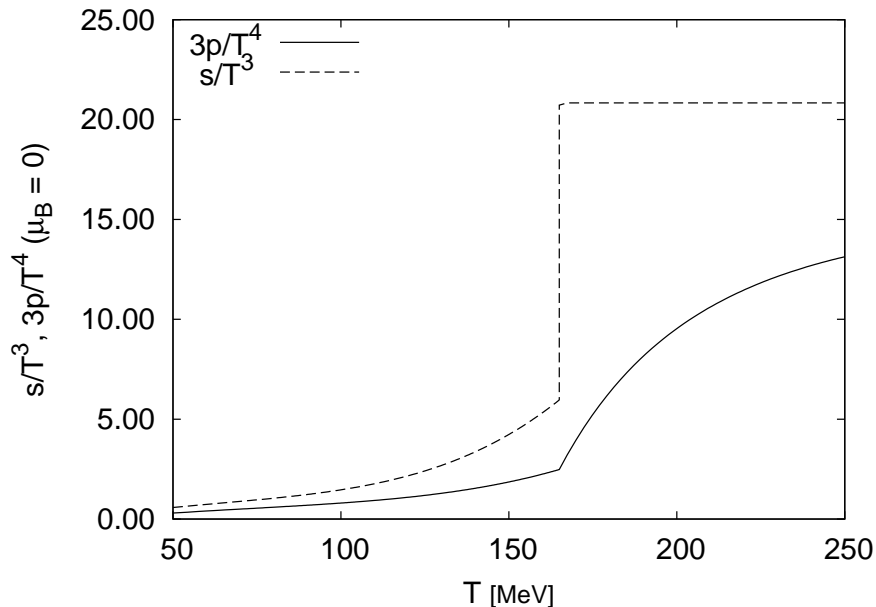
Figure 2.4: Pressure and entropy density as a function of temperature in the Bag model QGP + HRG EoS constructed here.

The phase transition temperature $T_c(\mu_B)$ is obtained from the phase coexistence condition. The value of T_c obviously depends on the choice of the Bag constant B in the QGP EoS. The Bag constant is chosen such that T_c is consistent with the lattice QCD results, at $\mu_B = 0$. In this work $T_c = 165$ MeV is used in all calculations. This procedure leads always to first order phase transition. Although the lattice QCD simulations suggest the transition to be a smooth cross-over at vanishing net-baryon number, the difference in hydrodynamics between the EoS here, with a first order phase transition, and a smooth but rapid cross-over such as in Ref. [70] is not very large. Indeed, the order of the phase transition has been shown to have only small effects on the transverse momentum spectra of hadrons and the elliptic flow of pions in the hydrodynamical model [71], especially when the decoupling temperature is kept as a free parameter. For quantities that are more sensitive to the detailed space-time evolution of the matter, a more detailed EoS should be considered. Actually a first order phase transition proceeds through nucleation and phase separation, but no macroscopic phase separation is present in the construction used here. This would require, *e.g.* a spinodal decomposition of the mixed phase [72]. In the construction used here, all hydrodynamical Fourier modes are either propagating or static, *i.e.* there are no exponentially growing unstable modes.

The resulting entropy density and pressure, as a function of temperature at $\mu_B = 0$, are shown in Fig. 2.4, scaled by the powers of temperature as indicated in the figure. The phase transition is visible as a discontinuity in
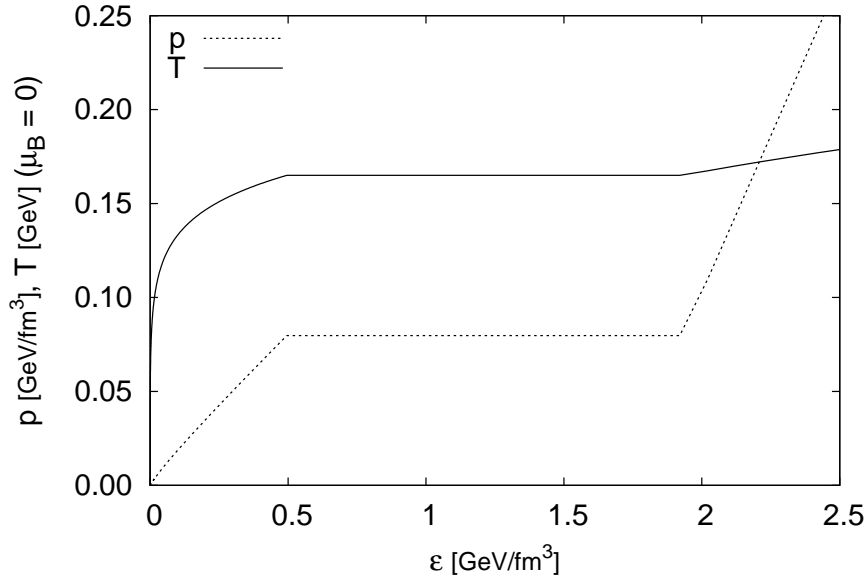
Figure 2.5: Pressure and temperature as a function of energy density in the Bag model QGP + HRG EoS.

the derivative of the pressure curve and as a sudden jump in the entropy density at T_c. The discontinuity in the entropy density indicates a sudden increase in the number of degrees of freedom in the matter. Although there are ~ 300 different hadronic states in the HRG, the effective number of degrees of freedom in the QGP is still considerably higher. Most of the hadronic states are strongly suppressed at these temperatures due to their large mass. In Fig. 2.5 the pressure and the temperature are shown as a function of the energy density at $\mu_B = 0$. The phase transition is seen as the constant pressure and temperature region. The latent heat of the transition can be read off from the figure as the width of the constant pressure (or temperature) region. In the hydrodynamical simulations collective flow is generated by the pressure gradients. Therefore the region of constant pressure, or slowly varying pressure in the case of a rapid cross-over transition, will have important effects on the hydrodynamical simulations, e.g. in suppressing the elliptic flow.

To solve the hydrodynamical equations, only the pressure as a function of the energy and baryon density is needed. One does not need to know the temperature or the degrees of freedom in the system. Thus it is not necessary to have a complete EoS in order to get information on the hydrodynamical behavior of the system. However, the treatment of the freeze-out requires knowledge about the degrees of freedom and for that information also the temperature and the chemical potentials are needed.

Although the model for the EoS considered here has several simplifi-

20

cations, it still catches the main properties of the QCD EoS: The correct degrees of freedom at low temperatures and QGP phase at the high temperatures, with the square of the speed of sound approaching $c_s^2 = 1/3$ when T increases. Also the Bag constant is chosen to be compatible with the critical temperature given by the lattice QCD simulations. These requirements are already restricting the EoS significantly.

Chapter 3

Numerical methods in hydrodynamics

Solving the hydrodynamical equations is a subject of its own and the calculational methods are still under active development. The method for solving Eqs. (2.28) and (2.31) which is used in this work, is introduced in this chapter. This method is called FCT–SHASTA [73, 74], where FCT stands for Flux Corrected Transport and SHASTA corresponds to SHArp and Smooth Transport Algorithm. The applicability of the method in the modeling of ultrarelativistic heavy ion collisions has been studied in Refs. [75, 76].

Typically a high-order accuracy in discretizing the transport equations is required to describe the evolution of hydrodynamic variables correctly. However, in the presence of large gradients, such as shock waves, high-order schemes can lead to strong dispersion of different Fourier modes, which in turn can cause unphysical ripples in the numerical solution and eventually invalidate the whole solution. On the other hand, this dispersion is not present in low-order schemes, but instead strong numerical diffusion can smooth out all structures from the solution and as such low-order schemes are not appropriate methods to be used for finding the solution in the whole space-time region. In the SHASTA algorithm this is solved by using a high-order method as long as it is not introducing any additional structures compared to the low-order method. When these structures tend to form, a combination of the low- and the high-order schemes is used in such a way that new structures will not form. In practice the low-order scheme is constructed in such a way that the explicit form of the numerical diffusion can be identified. High-order accuracy is then achieved by removing numerical diffusion from the low-order solution as much as possible, without forming new structures. The explicit form of this procedure for one and two spatial dimensions is given below.

3.1 SHASTA in one dimension

The SHASTA algorithm belongs to the class of finite-volume algorithms, where spatial derivatives are not discretized directly, but the solution is based on an explicit convection of the physical quantity from one cell to another. These kinds of methods explicitly conserve the quantities whose time evolution we wish to solve. The differential form of the conservation equation for a quantity ρ in one spatial dimension is given by

$$\partial_t \rho(x,t) + \partial_x \left(v_x \rho(x,t) \right) = C, \tag{3.1}$$

where v_x is the local flow velocity of ρ and C includes possible source terms. When $C = 0$ this equation expresses the local conservation of the quantity

$$R = \int_V dx \rho(x,t). \tag{3.2}$$

The integral form of the same conservation law for a cell with a volume V and a boundary S is given by

$$\frac{d}{dt} \int_V \rho dV + \int_S \hat{\mathbf{n}} \cdot \mathbf{F} dS = \int_V C dV, \tag{3.3}$$

where $\hat{\mathbf{n}}$ is the unit normal vector of the surface S and $\mathbf{F}$ is the flux density of the quantity R through the surface.

In the finite-volume approach, the space is divided into discrete cells where density and other variables are known at the node points, typically at the center of the cell. The SHASTA algorithm is divided into a transport part and a flux correction part. In the first stage of the transport part the originally piecewise constant distribution of the matter is approximated by piecewise linear distribution, as shown in Fig. 3.1. After this, each node point is moved by an amount $v_i \Delta t$, where v_i is the velocity of the matter at the node point (see Fig. 3.2). Between the node points the density is scaled in such a way that the total amount of matter is conserved *i.e.* density is multiplied by $\Delta x / \Delta x'$, where Δx is the original distance between the node points and $\Delta x'$ is the new distance. The new distribution of the matter is then divided into original cells to obtain a new piecewise-constant matter distribution shown in Fig. 3.3. This procedure leads to an expression for the updated density [73]:

$$
\begin{aligned}
\bar{\rho}_j^{n+1} &= \frac{1}{2} Q_-^2 \left(\rho_{j-1}^n - \rho_j^n \right) + \frac{1}{2} Q_+^2 (\rho_{j+1}^n - \rho_j^n) + (Q_+ + Q_-)\rho_j^n, \\
Q_\pm &= \frac{1/2 \mp \epsilon_j}{1 \pm (v_{j\pm 1} - v_j)\frac{\Delta t}{\Delta x}}, \\
\epsilon_j &= v_j \frac{\Delta t}{\Delta x}.
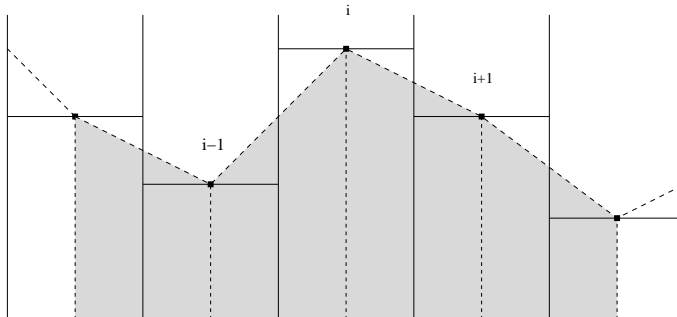\end{aligned}
\tag{3.4}
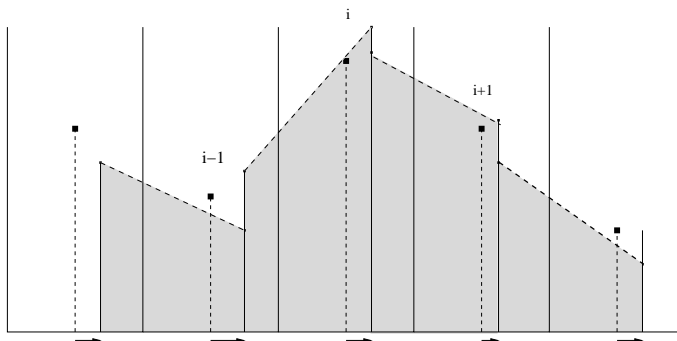$$

Figure 3.1: The SHASTA transport stage 1

Figure 3.2: The SHASTA transport stage 2

This algorithm clearly requires that

$$|\epsilon_j| = \left| v_j \frac{\Delta t}{\Delta x} \right| < \frac{1}{2}, \tag{3.5}$$

otherwise the node point would be moved out from the cell in Fig. 3.2. Going from a piecewise-constant profile in Fig. 3.1 to a piecewise-linear distribution introduces strong numerical diffusion of the matter from cell to cell. The advantage of the algorithm is that an explicit form of the diffusion can be obtained. From Eq. (3.4) by using a constant velocity $v_i = v$ one gets

$$\bar{\rho}_j^{n+1} = \rho_j^n + \frac{\epsilon}{2}(\rho_{j-1}^n - \rho_{j+1}^n) + \left(\frac{1}{8} + \frac{\epsilon^2}{2} \right) \left(\rho_{j+1}^n - 2\rho_j^n + \rho_{j-1}^n \right), \tag{3.6}$$

which includes a strong velocity-independent diffusion part. If the numerical diffusion is removed from the low-order solution, we get effectively a high-order solution. However, as explained above, this can lead to unphysical ripples in the solution. The main idea in the SHASTA algorithm is to remove the numerical diffusion as much as possible without generating extra ripples in the density distribution. In practice this is done by requiring that no new minima or maxima form when the diffusion is removed. If the updated
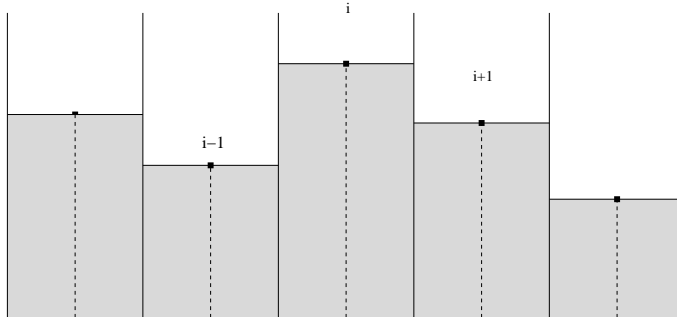
24

Figure 3.3: The SHASTA transport stage 3

density after the transport stage is denoted as $\tilde{\rho}_j^{n+1}$, the final density after the time-step is

$$\rho_j^{n+1} = \tilde{\rho}_j^{n+1} - A_j^c + A_{j-1}^c, \tag{3.7}$$

where A_j^c's are the antidiffusion fluxes. From Eq. (3.6) the numerical diffusion flux A_j is

$$A_j = \eta \left(\rho_{j+1}^{n+1} - \rho_j^{n+1} \right), \tag{3.8}$$

where η is the antidiffusion coefficient. The velocity-independent part of the flux is given by $\eta = 1/8$. In practice this value leads to unstable solutions. Therefore η is left as a free parameter. To prevent new minima or maxima, the antidiffusion flux is defined as

$$A_j^c = \text{sign}(A_i) \max(0, \min(A_{i-1}\text{sign}(A_{i+1}), \eta|A_{i+1}|, A_{i+2}\text{sign}(A_{i+1}))). \tag{3.9}$$

These fluxes are used in Eq. (3.6) to get the full solution of the transport part of Eq. (3.1). Source terms C are added to this solution. This is the form of the SHASTA algorithm which is used to solve the cylindrically symmetric, boost-invariant hydrodynamical Eqs. (2.31). A cylindrical geometry could also be embedded into the transport algorithm [77, 78], but this is not done here. Instead, the additional terms in Eqs. (2.31) arising from the cylindrical geometry are taken into account as source terms.

3.2   Two-dimensional flux limiter

Two-dimensional transport in the Cartesian coordinates is calculated by applying the one-dimensional algorithm (3.4) separately in both the x and y directions. The one-dimensional form of the flux limiter algorithm introduced above could be used in a similar way separately in both directions, but it would not prevent the occurrence of all possible new minimas or maximas at the antidiffusion stage. For this reason, a new flux limiter for multidimensional transport problems, which takes both dimensions simultaneously into account, was introduced by Zalesak [74]. In two dimensions

25

the antidiffusion fluxes are defined as

$$A_{i+1/2,j} = \eta(\tilde{\rho}_{i+1,j}^{n+1} - \tilde{\rho}_{i,j}^{n+1}), \tag{3.10}$$

where $\tilde{\rho}$ is the density after the transport stage without source terms. The next step is to define $\rho_{i,j}^{\min}$ and $\rho_{i,j}^{\max}$ in such a way that when $\rho_{i,j}^{\min} < \rho_{i,j} < \rho_{i,j}^{\max}$ new minima or maxima are not created. In the Zalesak algorithm these minimum and maximum densities are defined as

$$\begin{aligned}
\rho_{i,j}^a &= \max(\rho_{i,j}^n, \bar{\rho}_{i,j}^{n+1}), \\
\rho_{i,j}^{max} &= \max(\rho_{i-1,j}^a, \rho_{i,j}^a, \rho_{i+1,j}^a, \rho_{i,j-1}^a, \rho_{i,j+1}^a), \\
\rho_{i,j}^b &= \min(\rho_{i,j}^n, \bar{\rho}_{i,j}^{n+1}), \\
\rho_{i,j}^{min} &= \min(\rho_{i-1,j}^b, \rho_{i,j}^b, \rho_{i+1,j}^b, \rho_{i,j-1}^b, \rho_{i,j+1}^b),
\end{aligned} \tag{3.11}$$

where ρ^n is the density in the previous time-step and $\bar{\rho}^{n+1}$ is the density after the transport stage and the inclusion of pressure gradient terms. According to Zalesak, the antidiffusion flux into the directions of pressure gradients will enhance the minima and maxima. Therefore the first step in the flux limiting procedure is to set the antidiffusion flux to zero in such directions:

$$\begin{aligned}
A_{i+1/2,j} &= 0, \text{if } A_{i+1/2,j}(\bar{\rho}_{i+1,j}^{n+1} - \bar{\rho}_{i,j}^{n+1}) < 0 \\
&\text{and either } A_{i+1/2,j}(\bar{\rho}_{i+2,j}^{n+1} - \bar{\rho}_{i+1,j}^{n+1}) < 0 \\
&\text{or } A_{i+1/2,j}(\bar{\rho}_{i,j}^{n+1} - \bar{\rho}_{i-1,j}^{n+1}) < 0, \\
A_{i,j+1/2} &= 0, \text{if } A_{i,j+1/2}(\bar{\rho}_{i,j+1}^{n+1} - \bar{\rho}_{i,j}^{n+1}) < 0 \\
&\text{and either } A_{i,j+1/2}(\bar{\rho}_{i,j+2}^{n+1} - \bar{\rho}_{i,j+1}^{n+1}) < 0 \\
&\text{or } A_{i,j+1/2}(\bar{\rho}_{i,j}^{n+1} - \bar{\rho}_{i,j-1}^{n+1}) < 0,
\end{aligned} \tag{3.12}$$

where A's are calculated according to Eq. (3.10), *i.e.* without the pressure gradient terms, and $\bar{\rho}$'s include the pressure terms. For the flux limiting algorithm the following quantities are defined

$$\begin{aligned}
P_{i,j}^+ &= \sum(\text{all flux into the cell } (i,j)) \\
&= \max(0, A_{i-1/2,j}) - \min(0, A_{i+1/2,j}) + \max(0, A_{i,j-1/2}) - \min(A_{i,j+1/2}), \\
O_{i,j}^+ &= \rho_{i,j}^{max} - \bar{\rho}_{i,j}^{n+1}, \\
R_{i,j}^+ &= \begin{cases} \min(1, O_{i,j}^+/P_{i,j}^+), & \text{if } P_{i,j}^+ > 0 \\ 0 & \text{if } P_{i,j}^+ = 0 \end{cases}, \\
P_{i,j}^- &= \sum(\text{all flux out from the cell } (i,j)) \\
&= \max(0, A_{i+1/2,j}) - \min(0, A_{i-1/2,j}) + \max(0, A_{i,j+1/2}) - \min(A_{i,j-1/2}), \\
O_{i,j}^- &= \bar{\rho}_{i,j}^{n+1} - \rho_{i,j}^{min}, \\
R_{i,j}^- &= \begin{cases} \min(1, O_{i,j}^-/P_{i,j}^-), & \text{if } P_{i,j}^- > 0 \\ 0 & \text{if } P_{i,j}^- = 0 \end{cases}.
\end{aligned}$$

$$\tag{3.13}$$

The flux limiting is then imposed according to

$$C_{i+1/2,j} = \begin{cases} \min(R_{i+1,j}^+, R_{i,j}^-), & \text{if } A_{i+1/2,j} > 0 \\ \min(R_{i,j}^+, R_{i+1,j}^-), & \text{if } A_{i+1/2,j} < 0 \end{cases},$$

$$C_{i,j+1/2} = \begin{cases} \min(R_{i,j+1}^+, R_{i,j}^-), & \text{if } A_{i,j+1/2} > 0 \\ \min(R_{i,j}^+, R_{i,j+1}^-), & \text{if } A_{i,j+1/2} < 0 \end{cases}, \tag{3.14}$$

and the final antidiffusion fluxes after the flux limiting procedure are

$$\begin{aligned} A_{i+1/2,j}^c &= C_{i+1/2,j} A_{i+1/2,j}, \\ A_{i,j+1/2}^c &= C_{i,j+1/2} A_{i,j+1/2}. \end{aligned} \tag{3.15}$$

Finally the updated density is written as

$$\rho_{i,j}^{n+1} = \bar{\rho}_{i,j}^{n+1} - (A_{i+1/2,j}^c - A_{i-1/2,j}^c + A_{i,j+1/2}^c - A_{i,j-1/2}^c). \tag{3.16}$$

This procedure is still explicitly conservative. Any additional source terms are added to the density afterwards.

After the time-step we get new updated values for the tensor components T^{00} and T^{0i}. In relativistic hydrodynamics we still need to solve the local energy density separately, since the EoS is given as a function of ε and n_B, and not as a function of the tensor components. The local energy density is solved from

$$\varepsilon = T^{00} - \frac{(T^{0i})^2}{T^{00} + p(\varepsilon, n_B)}. \tag{3.17}$$

For a simple EoS $p = c_s^2 \varepsilon$, where c_s is a constant velocity of sound, this can be solved analytically, but in a general case some iterative procedure, such as Newton's method, is needed. Once ε is solved, the pressure is obtained from the EoS, and the flow velocity is calculated from

$$v^i = \frac{T^{0i}}{T^{00} + p}. \tag{3.18}$$

The algorithm described above leads to a high-order accuracy in the spatial discretization. Second-order accuracy in the time discretization is achieved by calculating first the half time-step values from t_i to $t_i + \Delta t/2$ by applying the SHASTA algorithm above. The complete time-step from t_i to $t_i + \Delta t$ is then taken by using the calculated half time-step values for the pressure and velocity in the algorithm.

Chapter 4

Decoupling and resonance decays

In the hydrodynamical modeling of ultrarelativistic heavy ion collisions, one of the problems is how to end the time-evolution of the system. Obviously the hydrodynamical evolution in a finite-size, strongly expanding system cannot continue forever. Eventually the system becomes so dilute that the particles cease to interact and therefore the system cannot stay in thermodynamical equilibrium, but becomes a system of free particles. Hydrodynamical models alone cannot predict when the system is going to decouple, but some additional knowledge of microscopical properties of the particle interactions is needed. Even if we knew when the decoupling is going to happen, it is still not an easy task to model the freeze-out process. In reality the freeze-out happens in a finite space-time region, *i.e.* it is not expected to be an instantaneous process. The whole process is a non-equilibrium process and the final free-particle distributions will most likely have some sensitivity to the details of the freeze-out mechanism.

In this work, however, we simply take the freeze-out to be an instantaneous process, in which free particles are emitted from a sharp boundary in space-time. The freeze-out can still happen at different times at different parts of the system, but locally the decoupling is always instantaneous. Typically the freeze-out boundary is obtained by specifying, *e.g.* the freeze-out temperature, *i.e.* from the hydrodynamical solution we search for a $T(\tau, x, y) = T_{\text{dec}}$ boundary and calculate the particle emission from this boundary. This is the approach in Refs [I, II, IV]. We studied in Ref. [III] a more dynamical freeze-out condition, *i.e.* the freeze-out boundary is obtained from the condition [79, 80, 81, 82, 83, 84]

$$\theta = c\Gamma, \tag{4.1}$$

where θ is the local expansion rate obtained from the hydrodynamical calculation and Γ is the local scattering rate of the particles. The constant c is

determined from experimental data, but it should be of order 1. Both ways of modeling the freeze-out are discussed below.

4.1 The Cooper-Frye decoupling

Regardless of whether the decoupling condition is specified by a constant T_{dec} or a constant c in the expression (4.1), we still need to model the particle emission from the decoupling boundary. In this work the modeling is according to the Cooper-Frye procedure [85], where the momentum distributions of particles are given by the thermal distribution and particle emission is obtained by counting the number of particles crossing the freeze-out boundary.

The decoupling boundary itself is a three-dimensional hypersurface in the four-dimensional Minkowski space. The surface elements of the decoupling surface in the boost-invariant hydrodynamical calculation are given by[1]

$$d\sigma_\mu = -[\pm]\left(\cosh\eta, -\frac{\partial\tau}{\partial x'}, -\frac{\partial\tau}{\partial y'}, -\sinh\eta\right)\tau d\eta dx' dy', \qquad (4.2)$$

where $[\pm]$ is defined as

$$[\pm] = \text{Sign}\left(\frac{\partial T}{\partial\tau}\right). \qquad (4.3)$$

This definition states that the normal vector of the surface is chosen in the direction of decreasing temperature. The particle 4-current is given by

$$j^\mu(x) = \int d^3\mathbf{p}\frac{p^\mu}{E}f(x,p), \qquad (4.4)$$

where $f(x,p)$ is the momentum distribution function of the particle, given in this case by the Fermi-Dirac or Bose-Einstein equilibrium distribution functions. The number of particles crossing the boundary σ can be calculated from

$$N = \int_\sigma j^\mu d\sigma_\mu = \int_\sigma d^3\mathbf{p}f(x,p)\frac{p^\mu}{E}d\sigma_\mu, \qquad (4.5)$$

where the integral is over the decoupling boundary σ. Using this expression and the equilibrium distribution functions the Cooper-Frye integral for the particle momentum spectrum becomes

$$E\frac{dN}{d^3\mathbf{p}} = \int_\sigma \frac{1}{(2\pi)^3}\frac{p^\mu d\sigma_\mu}{e^{(u\cdot p-\mu)/T}\pm 1}, \qquad (4.6)$$

where u is the fluid 4-velocity, μ is the chemical potential and T is the temperature. Thus, from the hydrodynamical evolution we must be able to determine the boundary σ itself and u, μ and T on the boundary.

---

[1]The derivation of the two-dimensional Cooper-Frye formula is here based on the notes by P.V. Ruuskanen.

Usually the momentum spectra are given as a function of transverse momentum p_T and rapidity y, defined as

$$y = \frac{1}{2} \ln \left(\frac{E + p_z}{E - p_z} \right).$$ (4.7)

With this definition, the particle energy E and the longitudinal momentum p_z are given by

$$E \quad = m_T \cosh y,$$ (4.8)
$$p_z \quad = m_T \sinh y,$$ (4.9)

where transverse mass is $m_T = \sqrt{m^2 + p_T^2}$. Thus the 4-momentum can be written as

$$p^\mu = (m_T \cosh y, \mathbf{p}_T, m_T \sinh y),$$ (4.10)

and the invariant spectrum as

$$E \frac{dN}{d^3\mathbf{p}} = \frac{dN}{dy d^2\mathbf{p}_T}.$$ (4.11)

In a longitudinally boost-invariant system, the fluid 4-velocity can be written in terms of the space-time rapidity η as

$$u^\mu = \gamma_T (\cosh \eta, \mathbf{v}_T, \sinh \eta),$$ (4.12)

where $\mathbf{v}_T$ is the transverse velocity and the transverse gamma factor is

$$\gamma_T = \frac{1}{\sqrt{1 - \mathbf{v}_T^2}}.$$ (4.13)

Using these in the Cooper-Frye formula and writing the momentum distribution as a geometrical series,

$$\frac{1}{e^x \pm 1} = \frac{e^{-x}}{1 \pm e^{-x}} = e^{-x} \sum_{n=0}^{\infty} (\pm)^n e^{-nx},$$ (4.14)

the integral can be written as

$$\frac{dN}{dy d^2\mathbf{p}_T} = \frac{1}{(2\pi)^3} \sum_{n=1}^{\infty} (\pm 1)^n \int_\sigma [\pm] \tau dx' dy' e^{n\mu/T} \exp \left(n\gamma_T \frac{\mathbf{v}_T \cdot \mathbf{p}_T}{T} \right)$$
$$\int d\eta \exp \left(-n\gamma_T \frac{m_T}{T} \cosh(\eta - y) \right) \left(m_T \cosh(\eta - y) - p_{x'} \frac{\partial \tau}{\partial x'} - p_{y'} \frac{\partial \tau}{\partial y'} \right).$$
(4.15)

Because $\mathbf{v}_T$ and T are independent of η, the η-integration can be carried out and the Cooper-Frye formula takes the form

$$
\frac{dN}{dyd^2\mathbf{p}_T} = \frac{1}{(2\pi)^3} \sum_{n=1}^{\infty} (\pm 1)^n \int_\sigma [\pm]\tau dx' dy' e^{n\mu/T} \exp\left(n\gamma_T \frac{\mathbf{v}_T \cdot \mathbf{p}_T}{T}\right)
$$
$$
\left[m_T K_1\left(n\gamma_T \frac{m_T}{T}\right) - \left(p_{x'}\frac{\partial\tau}{\partial x'} + p_{y'}\frac{\partial\tau}{\partial y'}\right) K_0\left(n\gamma_T \frac{m_T}{T}\right) \right],
\tag{4.16}
$$

where K_i's are the modified Bessel functions of the second kind. The remaining two-dimensional surface integral has to be done numerically. The integration can be performed by using the result $dx'(\partial\tau/\partial x') = d\tau$, which holds on the boundary. Thus, the second term can be expressed as an integral over y' and τ. Correspondingly, the third term can be written as an integral over x' and τ. In the integral $dx'dy'$ is always positive. The sign of the integration element must be determined by calculating $[\pm]$ explicitly.

For cylindrically symmetric systems, *i.e.* for central nucleus-nucleus collisions the formula (4.16) can still be simplified by writing it in cylindrical coordinates and performing the ϕ-integral. The result is the Cooper-Frye formula [54]

$$
\frac{dN}{dyd^2\mathbf{p}_T} = \frac{1}{2\pi^2} \int_\sigma \tau r \sum_{n=1}^{\infty} (\pm 1)^{n+1}
$$
$$
e^{n\mu/T}(m_T I_0(\frac{n}{T}p_T \sinh y_r) K_1(\frac{n}{T}m_T \cosh y_r) dr
\tag{4.17}
$$
$$
-p_T I_1(\frac{n}{T}p_T \sinh y_r) K_0(\frac{n}{T}m_T \cosh y_r) d\tau),
$$

where the transverse rapidity is defined as

$$
y_r = \frac{1}{2} \ln\left(\frac{1+v_r}{1-v_r}\right),
\tag{4.18}
$$

and I_i's are the modified Bessel functions of the first kind. All signs are correct when the integration is started from $(r = 0, \tau_{max})$, see *e.g.* the decoupling surfaces in Chap. 6.

4.2 Resonance decays

For consistency, the Cooper-Frye integrals have to be calculated for all particles included in the EoS. Most of these particles are, however, unstable and decay through strong or electromagnetic interactions, hence these particles are not directly detectable. To compare the calculated results with the experimental data, these decays have to be considered. There are ~ 300 different particle states included in the HRG, and each can have several different decay channels. In this work we limit the study to 2- and 3-particle

decays. The decays are calculated by assuming isotropic distribution of decay products in the rest frame of the decaying particle. Transverse momentum distribution of the decay products is obtained by folding the known momentum spectrum of the unstable particle with the single-particle decay distribution, and taking the integral over the allowed phase space [86, 87]. The single-particle decay distribution from a 2-particle decay is given by

$$dN = \frac{d\Gamma}{\Gamma},$$
(4.19)

where $d\Gamma$ is the differential decay width of the particle,

$$d\Gamma = \frac{d^3p_1}{2E_1}\frac{d^3p_2}{2E_2}\frac{g(M^2)}{2E}\delta^4(p - p_1 - p_1),$$
(4.20)

where E, p, and M are the energy, 4-momentum and mass of the decaying particle, and E_i and p_i are the energy and 4-momentum of the decay products and $g(M^2)$ is the squared matrix element for the decay, which is assumed to depend only on the mass of the particle. The decay rate Γ is obtained by integrating over the phase space of the decay products,

$$\Gamma = \frac{g(M^2)}{2E}\int \frac{d^3p_1}{2E_1}\frac{d^3p_2}{2E_2}\delta^4(p - p_1 - p_1).$$
(4.21)

The momentum spectra of the decay product 1 is obtained from these expressions as

$$E_1\frac{dN}{d^3p_1} = \frac{M}{4\pi p_{12}^* E_2}\delta(E - E_1 - E_2),$$
(4.22)

with $\mathbf{p}_2 = \mathbf{p} - \mathbf{p}_1$ and $E_2 = \sqrt{m_2^2 + \mathbf{p}_2^2}$. In the equation p_{12}^*, the cm momentum of decay particles, is defined as

$$p_{12}^* = \frac{\sqrt{(\tilde{m}^2)^2 - 4M^2 m_1^2}}{2M},$$
(4.23)

where

$$\tilde{m}^2 = M^2 + m_1^2 - m_2^2.$$
(4.24)

The momentum distribution of decay product 1 can be written as

$$E_1\frac{dN}{d^3p_1} = \int \frac{d^3p}{E}E\frac{dN}{d^3p}\frac{M}{4\pi p_{12}^* E_2}\delta(E - E_1 - E_2),$$
(4.25)

where $E\frac{dN}{d^3p}$ is the known distribution of the decaying particle. Equation (4.25) can be written as an integral over the transverse mass and rapidity,

$$E_1\frac{dN}{d^3p_1} = \frac{b_{12}M}{4\pi p_{12}^*}\int_{-\tilde{y}_{max}}^{\tilde{y}_{max}} \frac{d\tilde{y}}{\sqrt{m_{1T}^2\cosh^2\tilde{y} - p_{1T}^2}}\int_{M_T^-}^{M_T^+} \frac{M_T dM_T}{\sqrt{\left(M_T^+ - M_T\right)\left(M_T - M_T^-\right)}}$$

$$\left[\frac{dN}{dY dp_T^2 d\phi}|_{\phi=\phi_1-\theta} + \frac{dN}{dY dp_T^2 d\phi}|_{\phi=\phi_1+\theta}\right]_{p_T^2=M_T^2-M^2, Y=y_1-\tilde{y}},$$
(4.26)

where b_{12} is the branching ratio of the decay channel and θ is defined as

$$\cos\theta = -\frac{1}{2p_{1T}p_T}\left(\tilde{m}^2 - 2M_T m_{1T}\cosh(Y - y_1)\right). \qquad (4.27)$$

The integration limits for the M_T integral are calculated from

$$M_T^{\pm} = \frac{\tilde{m}^2 m_{1T}\cosh\tilde{y} \pm p_{1T}\sqrt{D}}{2(m_{1T}^2\cosh^2\tilde{y} - p_{1T}^2)}, \qquad (4.28)$$

where

$$D = (\tilde{m}^2)^2 - 4M^2(m_{1T}^2\cosh^2\tilde{y} - p_{1T}^2). \qquad (4.29)$$

The limit $\tilde{y}_{max}$ for the rapidity integral is given by

$$\tilde{y}_{max} = \operatorname{arcosh}\left(\frac{\sqrt{(\tilde{m}^2)^2 - 4M^2 p_{1T}^2}}{2M m_{1T}}\right). \qquad (4.30)$$

A three-particle decay can be reduced to a two-particle decay for the decay product we wish to calculate by treating the remaining two particles as a single particle with an invariant mass m_{23} integrated over the kinematically allowed phase-space. This procedure gives the decay distribution for the particle 1 in the three-particle decay as follows

$$
\begin{aligned}
E_1\frac{dN}{d^3p_1} &= \frac{b_{12}M^2}{\pi Q}\int_{m_2+m_3}^{M-m_1} dm_{23}\frac{\sqrt{(m_{23}^2 + m_2^2 - m_3^2)^2 - 4m_{23}^2 m_2^2}}{m_{23}} \\
&\int_{-\tilde{y}_{max}}^{\tilde{y}_{max}} \frac{d\tilde{y}}{\sqrt{m_{1T}^2\cosh^2\tilde{y} - p_{1T}^2}}\int_{M_T^-}^{M_T^+}\frac{M_T dM_T}{\sqrt{\left(M_T^+ - M_T\right)\left(M_T - M_T^-\right)}} \\
&\left[\frac{dN}{dY dp_T^2 d\phi}\Big|_{\phi=\phi_1-\theta} + \frac{dN}{dY dp_T^2 d\phi}\Big|_{\phi=\phi_1+\theta}\right]_{p_T^2=M_T^2-M^2, Y=y_1-\tilde{y}},
\end{aligned}
\qquad (4.31)
$$

where the integration limits are the same as for the two-particle decays, but m_2 is replaced by the invariant mass m_{23}. The normalization constant Q is calculated from

$$Q = \int_b^c \frac{dx}{x}\sqrt{a-x}\sqrt{b-x}\sqrt{x-c}\sqrt{x-d}, \qquad (4.32)$$

where

$$a = (M + m_1)^2, \quad b = (M - m_1)^2, \qquad (4.33)$$
$$c = (m_2 + m_3)^2, \quad d = (m_2 - m_3)^2. \qquad (4.34)$$

4.3 Dynamical decoupling condition

In the article [III] of this thesis we have studied also a more dynamical freeze-out condition. Instead of performing the freeze-out from a constant-temperature boundary, keeping the freeze-out temperature T_{dec} as a free parameter, the decoupling boundary is determined from the following dynamical condition

$$\theta(\mathbf{x}, t) = c\Gamma_\pi(T(\mathbf{x}, t)), \tag{4.35}$$

where θ is the local expansion rate of the matter and Γ_π is the pion scattering rate. The constant c is a free parameter determined from the available experimental data.

As discussed in the previous chapters, hydrodynamical modeling is based on the assumption of local thermal equilibrium. Physically, one expects this assumption to be valid when all the relevant microscopical time scales are much shorter than the macroscopical time scales. The macroscopical time scale of expansion is locally given by the expansion scalar $\theta = \partial_\mu u^\mu$, which gives the relative expansion rate of a volume of a fluid element, $\dot{V}/V$ [82]. Once the hydrodynamical solution is known, the local expansion rate can be easily calculated from the expression

$$\theta = \partial_\mu u^\mu = \frac{\partial \gamma_r}{\partial \tau} + \frac{\gamma_r}{\tau} + \frac{\partial(\gamma_r v_r)}{\partial r} + \frac{\gamma_r v_r}{r}. \tag{4.36}$$

The microscopical timescale is given by the interaction rate of the particles in the HRG. The dominant component in the HRG are pions, whose decoupling we are here primarily interested in. The scattering rate of pion can be approximated as

$$\Gamma_\pi = \sum_X n_X \sigma_{\pi X}(T), \tag{4.37}$$

where n_X is the density of particle species X and $\sigma_{\pi X}(T)$ is the average cross section for πX interaction at the temperature T. The sum is over all particle species in the HRG. The pion scattering rate is proportional to the density of thermal target particles, and because pions are the most abundant component in the HRG, $\pi\pi$ scattering is the dominant scattering channel that keeps the system in equilibrium. As suggested in Ref. [III], the thermally averaged $\pi\pi$ scattering cross section can be parametrized as

$$\sigma_{\pi\pi}(T) = \sigma_0 + \frac{CT^2}{(T - T_0)^2 + (\Delta/2)^2}, \tag{4.38}$$

where $\sigma_0 = 0.60 \, \text{fm}^2$, $C = 0.78 \, \text{fm}^2$, $T_0 = 105 \, \text{MeV}$ and $\Delta = 170 \, \text{MeV}$, which reproduces the result in Ref. [88] for the $T < T_c$ temperature range, relevant for the decoupling. The pion scattering rate can thus be approximated as

$$\Gamma_\pi \simeq n_\pi(T)\sigma_{\pi\pi}(T), \tag{4.39}$$

where $n_\pi(T)$ is the thermal density of pions with mass $m_\pi \sim 140$ MeV. Also other particles contribute to the scattering rate, but these can be thought to be effectively included in the constant c in Eq. (4.35). The contribution from the other particles to the pion scattering rate can be estimated to be much smaller than that from the $\pi\pi$ interactions: *e.g.* at $T = 150$ MeV the pion-nucleon contribution compared to that from $\pi\pi$ scatterings is approximately

$$\frac{n_N}{n_\pi}\frac{\sigma_{\pi N}}{\sigma_{\pi\pi}} \sim \frac{1}{15}\frac{30\text{mb}}{20\text{mb}} \sim \frac{1}{10} \sim 10\,\%. \tag{4.40}$$

Although the πN cross section is quite large, the density of nucleons is much smaller than that of pions, resulting in a contribution to the pion scattering rate of only $\sim 10\%$ compared with that from $\pi\pi$ scattering.

The situation would, of course, reverse if we were to study the microscopic decoupling dynamics of nucleons. In that case the scattering rate of nucleons would be proportional to the pion density $\Gamma_N \sim n_\pi \sigma_{\pi N} + \cdots$. This would lead to a much larger scattering rate per nucleon than per pion [81]. Obviously the condition (4.35) above for pions cannot be applied for the other hadrons as such, but a different condition for each hadron species should be constructed. This is not, however, discussed here further, but we consider the dynamical freeze-out condition only for pions.

Chapter 5

Initial state for the hydrodynamical evolution

In the boost-invariant, perfect-fluid hydrodynamics the initial energy density and the net-baryon density in the transverse plane have to be obtained from outside. A large fraction of the work presented in this thesis is based on the initial state calculated from the EKRT model [14], which applies to central collisions. Our extension to noncentral collisions is based on the optical Glauber model, see *e.g.* Refs. [89, 90].

5.1 The Glauber model

The optical Glauber model for nucleus-nucleus collisions is based on the assumption that each nucleon travels along straight-line trajectories and it is also assumed that the cross section for each nucleon-nucleon collision remains unchanged, even if the nucleons have already collided. In the Glauber model, the total cross section for an $A + B$ collisions is given by

$$\sigma_{AB} = \int d^2\mathbf{b} \left(1 - \left(1 - \frac{\sigma_{NN} T_{AB}(\mathbf{b})}{AB} \right)^{AB} \right) \simeq \int d^2\mathbf{b} \left(1 - e^{-\sigma_{NN} T_{AB}(\mathbf{b})} \right),$$
(5.1)

where σ_{NN} is the cross section for inelastic nucleon-nucleon collisions, $\mathbf{b}$ is the impact parameter and T_{AB} is the standard nuclear overlap function, defined as

$$T_{AB}(\mathbf{b}) = \int d^2\mathbf{r} \ T_A(\mathbf{r} + \mathbf{b}/2) T_B(\mathbf{r} - \mathbf{b}/2),$$
(5.2)

with $T_A(\mathbf{r})$ denoting the nuclear thickness function, which is an integral over the longitudinal coordinate z of the nuclear density function,

$$T_A(\mathbf{r}) = \int dz \ \rho_A(\mathbf{r}, z).$$
(5.3)

In this work the nuclear density is parametrized with the Woods-Saxon profile

$$\rho_A(\mathbf{r}, z) = \frac{\rho_0}{\exp\left(\frac{r - R_A}{d}\right) + 1}, \tag{5.4}$$

with $d = 0.54$ fm and $\rho_0 = 0.17$ fm^{-3}. The nuclear radius R_A is calculated from the expression

$$R_A = 1.12 \, A^{1/3} - 0.86 \, A^{-1/3}. \tag{5.5}$$

In the Glauber model the transverse density of binary nucleon-nucleon collisions is given by

$$n_{BC}(\mathbf{r}, \mathbf{b}) = \sigma_{NN} T_A(\mathbf{r} + \mathbf{b}/2) T_B(\mathbf{r} - \mathbf{b}/2). \tag{5.6}$$

The number density of the nucleons participating in the nuclear collision, the wounded nucleon transverse density, is given by

$$\begin{aligned}
n_{WN}(\mathbf{r}, \mathbf{b}) = &\, T_A(\mathbf{r} + \mathbf{b}/2) \left[1 - \left(1 - \sigma_{NN} \frac{T_B(\mathbf{r} - \mathbf{b}/2)}{B} \right)^B \right] \\
&+ T_B(\mathbf{r} - \mathbf{b}/2) \left[1 - \left(1 - \sigma_{NN} \frac{T_A(\mathbf{r} + \mathbf{b}/2)}{A} \right)^A \right].
\end{aligned} \tag{5.7}$$

The integrals of $n_{WN}(\mathbf{r}, \mathbf{b})$ and $n_{BC}(\mathbf{r}, \mathbf{b})$ over the transverse plane, $\int d^2\mathbf{r}$, give the number of participants $N_{\text{part}}(\mathbf{b}) = N_{WN}(\mathbf{b})$ and the number of binary collisions $N_{BC}(\mathbf{b})$, respectively.

5.2 The EKRT model

The EKRT model developed in [14] is a model for the initial particle production in central ultrarelativistic $A+A$ collisions. It is based on the assumption that the low-p_T particle production is controlled by the saturation among the produced gluons. When the particle production starts, the high-p_T particles are formed before the low-p_T particles. The high-p_T particles start to fill the transverse area, πR_A^2, of the collision zone and eventually at some p_T the whole transverse plane is filled with the produced gluons. Subsequently, non-linearities predicted by QCD, gluon fusions, are expected to become important. When this happens the particle production saturates, $i.e.$ further growth of particle production is strongly inhibited. The key quantity in the EKRT model is the number of gluons, $N_{AA}(A, \sqrt{s}, \Delta y, p_0)$, produced with $p_T \geq p_0$ into a rapidity window Δy, which obviously depends on the collision energy $\sqrt{s_{NN}}$ and the nuclear mass number A. As long as $p_0 \gg \Lambda_{\text{QCD}}$ the number of gluons produced can be calculated from collinearly factorized

perturbative QCD. The saturation condition for central $A + A$ collisions can be written as [14]

$$N_{AA}(A, \sqrt{s}, \Delta y, p_0)\frac{\pi}{p_0^2} = c\pi R_A^2, \tag{5.8}$$

where π/p_0^2 is the transverse area occupied by each produced gluon. The constant of proportionality is set to $c = 1$. This condition determines the saturation momentum $p_0 = p_{sat}(A, \sqrt{s})$. Once p_{sat} is determined, the total number of particles, N^f of type f, produced into the rapidity window Δy, can be estimated as the number of particles with $p_T \geq p_{sat}$ alone,

$$N^f(A, p_0, \Delta y, \sqrt{s}) = T_{AA}(\mathbf{0})\sigma\langle N^f \rangle_{\Delta y, p_0}, \tag{5.9}$$

where $\sigma\langle N^f \rangle_{\Delta y, p_0}/\sigma_{NN}$ is the number of particles with $p_T \geq p_{sat}$, produced per binary nucleon-nucleon collision. The total transverse energy of the produced minijets is

$$E_T^f(A, p_0, \Delta y, \sqrt{s}) = T_{AA}(\mathbf{0})\sigma\langle E_T^f \rangle_{\Delta y, p_0}, \tag{5.10}$$

where $\sigma\langle E_T^f \rangle_{\Delta y, p_0}/\sigma_{NN}$ is the transverse energy produced per binary collision, see [II]. The initial energy density at the time of formation, $\tau_0 = 1/p_{sat}$, can be estimated from the transverse energy produced in Δy as

$$\varepsilon(\tau_0, \mathbf{r}) = \frac{dE}{dV} \approx \frac{dE_T}{\tau_0 d\eta d^2\mathbf{r}} = T_A(\mathbf{r})T_A(\mathbf{r})\frac{\sigma\langle E_T \rangle_{\Delta y, p_0}}{\tau_0 \Delta y}, \tag{5.11}$$

where the volume element reads $dV = dz d^2\mathbf{r} = \tau_0 d\eta d^2\mathbf{r} \simeq \tau_0 \Delta y d^2\mathbf{r}$. The model also gives an estimate for the net-baryon density as

$$n_B(\tau_0, \mathbf{r}) = \frac{dN^{B-\overline{B}}}{\tau_0 d\eta d^2\mathbf{r}} = T_A(\mathbf{r})T_A(\mathbf{r})\frac{\sigma\langle N^{B-\overline{B}} \rangle_{\Delta y, p_0}}{\tau_0 \Delta y}, \tag{5.12}$$

where $N^{B-\overline{B}}$ is calculated from the number of quarks and anti-quarks produced in Δy [II].

The pQCD particle production in the transverse plane is clearly proportional to the density of binary collisions $n_{BC}(\mathbf{r}, \mathbf{b})$ when there is only one scale p_{sat} which is the same in the whole nuclear overlap region. In principle p_{sat} is different in different transverse locations and this would modify the matter distribution [91, 92]. However, in this work we do not apply a local saturation condition, but all the results are based on the average saturation momentum p_{sat} given by Eq. (5.8). The uncertainty resulting from the initial distribution of the matter is estimated by considering also initial profiles which are proportional to the wounded nucleon density $n_{WN}(\mathbf{r}, \mathbf{b})$, keeping the same initial entropy as with the profile determined from Eq. (5.11). The EKRT model requires that $p_{sat} \gg \Lambda_{QCD}$, *i.e.* that QCD perturbation theory

38

must be applicable. In practice, this limits the use of the EKRT model to central or nearly central collisions. For noncentral collisions further assumptions and modeling are needed.

Hydrodynamical modeling requires that the matter is close to local thermal equilibrium throughout the evolution. According to the EKRT model the production time of the initial state is $\tau_0 = 1/p_{\text{sat}}$. To apply this initial state directly to the hydrodynamical models, an assumption of immediate thermalization is needed, *i.e.* it is assumed that the energy density given by Eq. (5.11) is the thermal energy density with thermodynamical pressure and temperature.

In this work two collision systems are studied. First the model is tested in the $\sqrt{s_{NN}} = 130$ and 200 GeV Au + Au collisions at RHIC, and then the predictions for the $\sqrt{s_{NN}} = 5.5$ TeV Pb + Pb collisions at the LHC are given. The initial state parameters for the two collision systems are given in Table 5.1.

	RHIC	LHC
$\sqrt{s_{NN}}$ [GeV]	200	5500
τ_0 [fm]	0.17	0.097
$\sigma\langle E_T\rangle$ [GeV mb]	83.6	468
$\sigma\langle N^{B-\overline{B}}\rangle$ [mb]	0.520	0.106
σ_{NN} [mb]	42	60

Table 5.1: The initial-state parameters for Au + Au collisions at RHIC and Pb + Pb at the LHC.

5.3   Noncentral collisions

Once the initial state in central nuclear collisions is obtained from the EKRT model, the centrality dependence of the initial state is modeled by two Glauber model limits. The initial energy density and net-baryon density are either assumed to be proportional to the density of binary collisions or to the density of wounded nucleons in the transverse plane, *i.e.* the energy density as a function of the impact parameter is constructed as

$$\varepsilon_{BC}(\mathbf{r}, \mathbf{b}) = C_{BC}\, n_{BC}(\mathbf{r}, \mathbf{b}), \tag{5.13}$$
$$\varepsilon_{WN}(\mathbf{r}, \mathbf{b}) = C_{WN}\, n_{WN}(\mathbf{r}, \mathbf{b}), \tag{5.14}$$

and similarly for the net-baryon density. In both cases the proportionality constant C is fixed in $b = 0$ collisions from the EKRT model in such a way that the initial entropy $dS/d\eta$ is the same as predicted by Eq. (5.11). The initial time in non-central collisions is taken to be the same as in central collisions. These two limits correspond to the eBC and eWN models in

Ref. [13]. The resulting initial states for the Au + Au collisions at RHIC are shown in Fig. 5.1 and for the Pb + Pb collisions at the LHC in Fig. 5.2 for selected centralities. These figures show the energy density profiles in the x- and y-directions. The impact parameter is chosen to be in the x-direction.
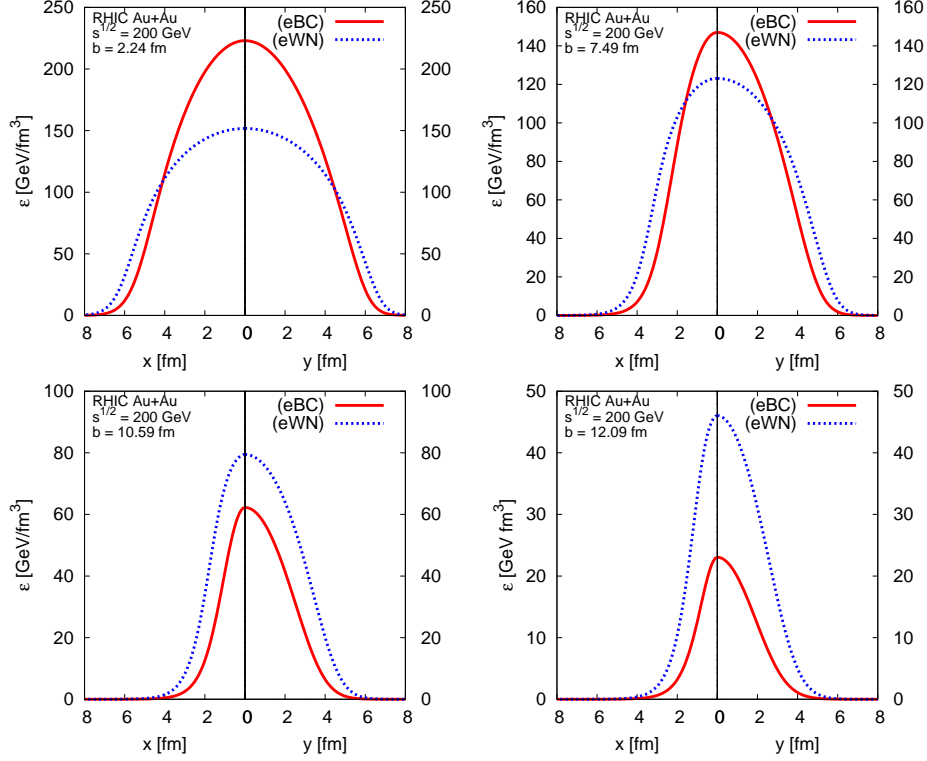

Figure 5.1: The transverse profiles of the initial energy density from the eBC and eWN initializations in $\sqrt{s_{NN}} = 200$ GeV Au + Au collisions at RHIC for different centralities. The energy density is shown in the x- and y-directions.

There are two main differences between the centrality dependence of the eBC and eWN models. First, the total entropy, and therefore also the final hadron multiplicity, falls faster with increasing b in the eBC initialization than in the eWN initialization. This is shown in Fig. 5.3, where the centrality dependence of the number of binary collisions and of wounded nucleons, both normalized to unity at $b = 0$ fm, are plotted. The second difference is that the eBC initialization results in much stronger energy density gradients, and thus also in stronger transverse pressure gradients in the transverse plane than the eWN initialization, as can be seen in Figs. 5.1 and 5.2. Since the pressure gradients are the driving force for the hydrodynamical evolution, the transverse flow develops faster with the eBC than with the eWN initial profile.

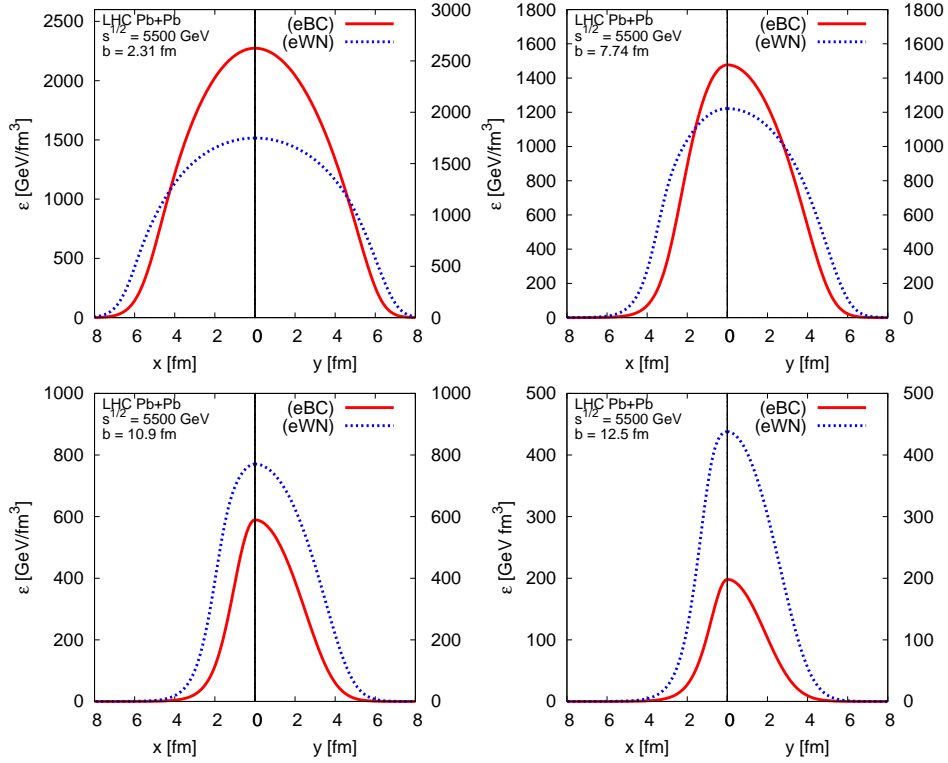It should be emphasized that we are not trying to find a detailed fit

Figure 5.2: The transverse profiles of the initial energy density from the eBC and eWN initializations in $\sqrt{s_{NN}} = 5500$ GeV Pb + Pb collisions at the LHC.

to the RHIC data. Instead we will show that towards peripheral collisions the measured final hadron transverse momentum spectra fall between the results obtained with the two chosen centrality dependences, and take the difference between them to represent the uncertainty in the extrapolation to the LHC energies. The centrality dependence of hadron multiplicity at RHIC could be fitted *e.g.* by taking a linear combination of the eBC and eWN initialization [13]. Alternatively one could use impact parameter dependent proportionality constants in Eqs. (5.13) and (5.14), like done, *e.g.* in Refs. [63, 71]. However, these fit parameters can change from RHIC to the LHC and an uncertainty in the extrapolation would remain anyway.

5.4 Centrality selection

The impact parameter is not a directly observable quantity, thus determining the centrality of the collision requires further modeling. The standard way to determine the centrality is through the Glauber model, in which the nuclear collisions can be divided into different centrality classes c_i according
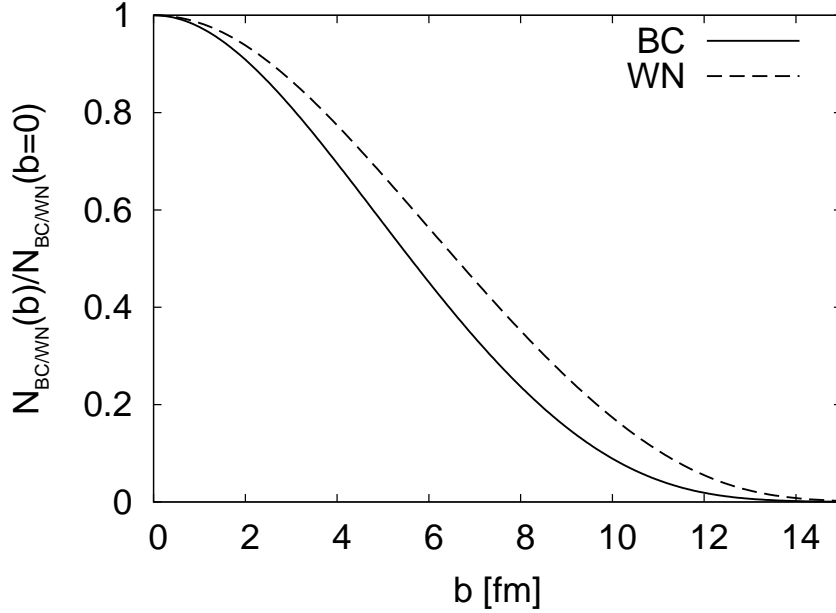
Figure 5.3: The relative number of binary collisions and of wounded nucleons as a function of the impact parameter in $\sqrt{s_{NN}} = 200$ GeV Au+Au collisions at RHIC.

	RHIC		LHC	
centrality %	b [fm]	N_{part}	b [fm]	N_{part}
0-5	2.24	347	2.31	374
5-10	4.09	289	4.23	315
10-15	5.30	242	5.47	264
15-20	6.27	202	6.48	221
20-30	7.49	153	7.74	168
30-40	8.87	102	9.17	112
40-60	10.6	50.8	10.9	56.7
60-70	12.1	19.6	12.5	21.2
70-80	13.0	9.13	13.4	9.65

Table 5.2: The average values of impact parameters and the average numbers of participants in selected centrality classes from the optical Glauber model in $\sqrt{s_{NN}} = 200$ GeV Au+Au collisions at RHIC and in $\sqrt{s_{NN}} = 5500$ GeV Pb+Pb collisions at the LHC.

to their contribution to the total cross section. For instance, the most central collision class c_0 can be defined to be those central collisions that contribute 5% to the total $A + A$ cross section,

$$0.05 = \frac{1}{\sigma_{AA}} \int_0^{b_1} d^2\mathbf{b} \frac{d\sigma_{AA}}{d^2\mathbf{b}}, \tag{5.15}$$

which in turn determines the impact parameter range $[0, b_1]$ that corresponds to the most central class. Other centrality classes can then be defined accordingly, *e.g.* the next centrality class can be defined to correspond to $5 - 15\%$ of the total cross section:

$$0.10 = \frac{1}{\sigma_{AA}} \int_{b_1}^{b_2} d^2\mathbf{b} \frac{d\sigma_{AA}}{d^2\mathbf{b}}, \quad (5.16)$$

which defines the b range $[b_1, b_2]$ that corresponds to this centrality class. Experimentally the same procedure can be implemented through some appropriate quantity which on the average decreases monotonically as a function of increasing b, like the total multiplicity or the total transverse energy produced in the collision. For each centrality class we can define the averages $\langle b \rangle$ and $\langle N_{WN} \rangle$ as weighted averages:

$$\langle b \rangle = \frac{1}{\sigma_{c_i}} \int_{b_i}^{b_{i+1}} d^2\mathbf{b}\, b \frac{d\sigma_{AA}}{d^2\mathbf{b}}, \quad (5.17)$$

$$\langle N_{WN} \rangle = \frac{1}{\sigma_{c_i}} \int_{b_i}^{b_{i+1}} d^2\mathbf{b}\, N_{WN}(\mathbf{b}) \frac{d\sigma_{AA}}{d^2\mathbf{b}}, \quad (5.18)$$

where

$$\sigma_{c_i} = \int_{b_i}^{b_{i+1}} d^2\mathbf{b} \frac{d\sigma_{AA}}{d^2\mathbf{b}}. \quad (5.19)$$

The average impact parameters and the average number of participants are shown in Table 5.2 for selected centrality classes. In practice, the hydrodynamical evolution of collisions in a given centrality class is calculated by using a fixed impact parameter given by Eq. (5.17).

Chapter 6

Hydrodynamical flow and hadron spectra

The space-time evolution of the matter and hadron spectra in different collision systems is obtained from the hydrodynamical model presented in Chaps 2, 4 and 5. The hydrodynamical evolution itself is not directly observable, and therefore it is important to understand the correlations between the hadron spectra and the hydrodynamical flow. The key observables obtained from the model are the total hadron multiplicity, which is dictated by the initial entropy, and the transverse momentum spectra of the hadrons, which in turn depend sensitively on the hydrodynamical flow field generated during the evolution.

In the boost-invariant approximation the p_T spectra are independent of rapidity. The variables we consider are the transverse momentum p_T and the azimuthal angle ϕ. In central collisions the initial state is azimuthally symmetric and therefore the spectra calculated from the model are also independent of ϕ. On the other hand, the initial state in non-central collisions is non-symmetric, and the p_T spectra become ϕ dependent.

Instead of giving the azimuthal dependence of the spectra explicitly in terms of ϕ, the dependence is usually quantified by the Fourier decomposition of the spectra [93],

$$\frac{dN(b)}{dydp_T^2 d\phi} = \frac{dN(b)}{dydp_T^2} \left[1 + 2v_1(y, p_T; b)\cos\phi + 2v_2(y, p_T; b)\cos(2\phi) + \cdots\right].$$

(6.1)

The rapidity and transverse momentum dependent Fourier coefficients are given by

$$v_n(y, p_T; b) \equiv \left(\frac{dN}{dydp_T^2}\right)^{-1} \int_{-\pi}^{\pi} d\phi \cos(n\phi)\frac{dN(b)}{dydp_T^2 d\phi},$$

(6.2)

where b is the average impact parameter corresponding to a given centrality

class. Similarly, the p_T-integrated coefficients v_n are given by

$$v_n(y; b) \equiv \left(\frac{dN(b)}{dy}\right)^{-1} \int_{-\pi}^{\pi} d\phi \cos(n\phi) \frac{dN(b)}{dy d\phi}. \qquad (6.3)$$

In the boost-invariant approximation the coefficients v_n are rapidity independent. A non-zero v_2 is usually called elliptic flow, since it is a result from an azimuthally anisotropic flow field in hydrodynamical models.

6.1 Hadron multiplicity

The total number of hadrons produced in the perfect-fluid hydrodynamical model depends on the following four quantities:

- the initial entropy density $dS/d\eta$,

- the degrees of freedom in the HRG,

- the decoupling temperature,

- the resonance decays.

The perfect-fluid hydrodynamics conserves entropy, therefore the final observed multiplicity depends on the number of hadrons per unit entropy n_h/s at the freeze-out. For massless particles this ratio is different for bosons and fermions, but it is independent of temperature. In such a case the multiplicity would be uniquely determined from the initial entropy. For massive particles, however, this ratio is not constant anymore, but depends on the temperature and the mass of the particle. Thus, during the hydrodynamical evolution of the HRG, hadron number is not conserved. However, when the decoupling temperature is fixed, the multiplicity is uniquely determined by the initial entropy.

On the other hand, the ratio n_h/s determines only the multiplicity of thermally emitted hadrons (see the Cooper-Frye integrals in Chap. 4). Most of the particles included in the HRG are unstable and will decay before they are observed. It turns out that for the pions the sum of thermal pions plus pions from the decays of unstable particles remains constant within 10% independent of the freeze-out temperature [I]. In this sense the pion number is conserved in the hydrodynamical evolution. This is clearly a property of the hadron mass-spectrum and decay channels rather than a thermodynamical property of the HRG, and it holds only for pions. In summary, if the HRG EoS is used, the final pion multiplicity is determined from the initial state alone whereas, for other, more massive hadrons the multiplicity depends strongly on the decoupling temperature.

6.2 Slopes of the transverse momentum spectra

In a static medium in thermodynamical equilibrium, the transverse momentum spectra are given by the Fermi-Dirac and Bose-Einstein distribution functions. At $p_T \gg m$ these distribution functions behave as $e^{-p_T/T}$. If there is no transverse flow, the slopes of the spectra are determined by the temperature alone. However, during the hydrodynamical evolution a strong transverse flow is generated and this affects the slopes. In the presence of the transverse hydrodynamical flow, at $\eta = 0$, $u^\mu = \gamma(1, \mathbf{v}_T, v_z) = \gamma(1, \mathbf{v}_T, 0)$ the high-p_T spectra behave approximately as

$$e^{-u \cdot p/T} = e^{-p_T/T_{\mathrm{eff}}}, \tag{6.4}$$

where T_{eff} is defined as

$$T_{\mathrm{eff}} = T \sqrt{\frac{1 + v_T}{1 - v_T}}. \tag{6.5}$$

When the matter decouples, different transverse flow velocities occur at different regions on the decoupling surface. Therefore, v_T in Eq. (6.5) is an effective flow velocity. If the decoupling is chosen to happen at a fixed temperature $T = T_{\mathrm{dec}}$, then a decrease in decoupling temperature leads to a longer lifetime of the hydrodynamical system, which in turn leads to a larger transverse flow on the lower-temperature decoupling surface. This is illustrated in Fig. 6.1, where the left-hand side shows the phase boundaries and two isotherms, $T = 150$ MeV and $T = 120$ MeV, and the right-hand side shows the transverse velocity along the isotherms from the hydrodynamical simulation of central Au + Au collision at RHIC. Also the flowlines starting from $r = 0, 1, \ldots, 7$ fm are shown in the figure. If the flow velocity increases at the same time as the temperature decreases, the net effect on the effective temperature depends on how v_T changes as a function of the decoupling temperature. For the EoS considered here, with the full kinetic and chemical equilibrium, it turns out that the increase in v_T wins over the decrease in temperature [I]. This can be seen in Fig. 6.2, which shows the pion, kaon and proton spectra from the hydrodynamical calculation illustrated in Fig. 6.1. As can be seen, the slopes of the p_T spectra depend strongly on the decoupling temperature.

Another property of the slopes of the p_T spectra is that at low p_T the slopes depend on the hadron mass. In the hydrodynamical system the flow velocity is common for all hadrons. Therefore heavier particles pick up more momentum from the flow field than the lighter ones. This leads to flatter spectra for the heavier particles, as can also be seen in Fig. 6.2.

6.3 Elliptic flow

In non-central collisions the initial state is azimuthally anisotropic in the transverse plane, as can be seen in Figs. 5.1 and 5.2. This anisotropy and
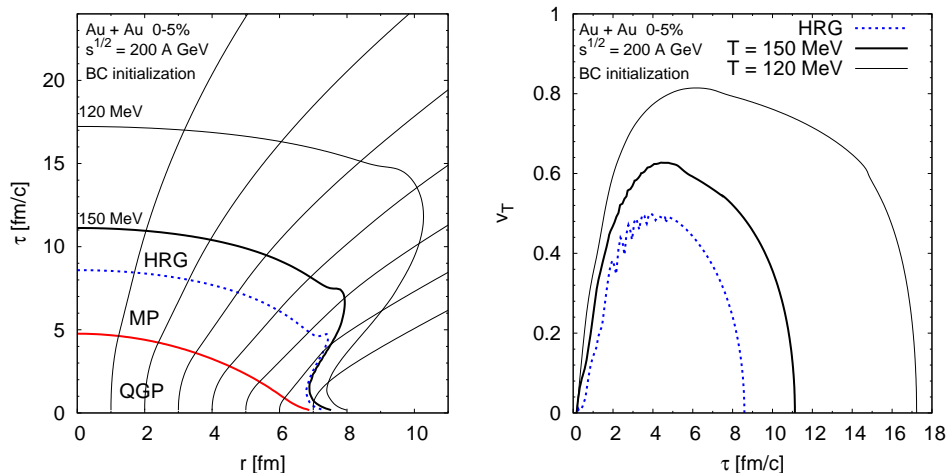
46

Figure 6.1: **Left:** The phase boundaries and two isotherms, $T = 150$ MeV and $T = 120$ MeV, in $0-5\,\%$ most central Au+Au collisions at RHIC. Also the flowlines starting from $r = 0, 1, \ldots, 7$ fm are shown. **Right:** Transverse velocity as a function of τ, along the mixed phase-HRG boundary and along the two isotherms shown in the left panel.

its time-evolution can be quantified by the spatial eccentricity defined as [23]

$$\varepsilon_x \equiv \frac{\langle y^2 - x^2 \rangle}{\langle y^2 + x^2 \rangle} \equiv \frac{\int dxdy\, \epsilon(x, y, \tau)(y^2 - x^2)}{\int dxdy\, \epsilon(x, y, \tau)(y^2 + x^2)}, \qquad (6.6)$$

where the integral is over the transverse plane and the energy density ϵ is used as a weighting factor. A spatially anisotropic distribution of the matter leads to anisotropic pressure gradients. Since the pressure gradients are the driving force for the hydrodynamic evolution, anisotropic pressure gradients will generate an anisotropic transverse flow field. A convenient way to characterize the anisotropy of the flow is through the momentum space eccentricity, which can be defined as [23]

$$\varepsilon_p \equiv \frac{\int dxdy\, (T^{xx} - T^{yy})}{\int dxdy\, (T^{xx} + T^{yy})}, \qquad (6.7)$$

where T^{ii} are the components of the energy-momentum tensor. A non-zero ε_p at the end of the hydrodynamical evolution converts to a non-zero v_2 extracted from the hadron spectra. A nice feature of this definition of ε_p is that it is, at the end of the time-evolution, approximately twice the final p_T-integrated v_2 of pions [23]. The pressure gradients will generate transverse flow, regardless whether they are asymmetric or not. The average transverse
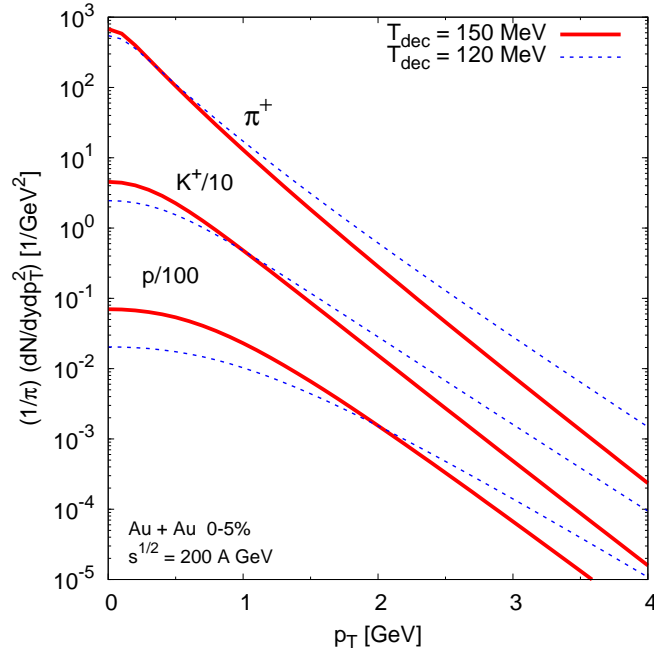
47

Figure 6.2: Transverse momentum spectra of positive pions, positive kaons and protons in $0 - 5$ % most central Au + Au collisions at RHIC at $\sqrt{s_{NN}} = 200$ GeV, for two different decoupling temperatures. The contributions from the strong and electromagnetic decays of unstable hadrons are included in the spectra.

flow can be defined as [23]

$$\langle v_T \rangle \equiv \frac{\langle \gamma v_T \rangle}{\langle \gamma \rangle} \equiv \frac{\int dx dy \, \epsilon(x, y, \tau) \gamma v_T(x, y, t)}{\int dx dy \, \epsilon(x, y, \tau) \gamma}, \qquad (6.8)$$

where the γ factor is used as an additional weight.

Initially both ε_p and $\langle v_T \rangle$ are always assumed to be zero, but in non-central collisions ε_x is not. The sign convention is chosen such that an initially positive ε_x leads to a positive ε_p, which in turn converts to a positive v_2. Figures 6.3 and 6.4 show the time evolution of the three quantities, defined above, for three different centralities at RHIC and the LHC, respectively. In addition, the phase boundaries and the $T = 150$ MeV isotherm are shown for each centrality.

The initially positive ε_x starts to decrease when the generated asymmetric flow field tends to drive the system towards azimuthally symmetric distribution of the matter. Thus the driving force for the increase of the elliptic flow is strongest during the early stages of the evolution. The spatial eccentricity will eventually go to zero and even to negative values. When the driving force disappears, ε_p saturates. Thus the elliptic flow measures the pressure in the early stages of the evolution [94], and the elliptic flow

48

coefficients measured at RHIC have been argued to point towards early thermalization of the QGP [23]. However, at some point of the evolution the phase transition from the QGP to the HRG takes place. The EoS we use has a first order phase transition, with a mixed phase between these phases. During the mixed phase the pressure is practically constant.[1] Therefore, all pressure gradients vanish and transverse flow stops increasing. Thus the amount of elliptic flow generated during the time-evolution is not limited only by ε_x, but it also depends on the lifetime of the QGP phase. At the collision energies studied here most of the matter is in mixed phase or in the HRG before the spatial eccentricity goes to zero, and the main factor limiting the amount of elliptic flow is the lifetime of the QGP phase (see Figs. 6.3 and 6.4). Although the initial spatial eccentricities are similar at the LHC and RHIC, the lifetime of the QGP phase is longer at the LHC. Therefore also ε_p at the end of the evolution is much larger than at RHIC.

One way to quantify how much initial spatial eccentricity is converted to the momentum space eccentricity is to plot v_2/ε_x, where v_2 is the p_T-integrated elliptic flow coefficient of pions as a function of the number of participants for different decoupling temperatures. This is shown in Fig. 6.5 for both the RHIC and LHC collision energies. As can be seen, at RHIC there is still sensitivity on the decoupling temperature, indicating that not all spatial asymmetries have disappeared before the matter enters the HRG. In contrast, at the LHC the ratio is almost independent of the temperature, except for the very peripheral collisions. This indicates that at the LHC the p_T-integrated v_2 is less sensitive to the details of the HRG dynamics than at RHIC.

---

[1]The pressure is strictly constant during the phase transition only at $\mu_B = 0$, but since both at RHIC and the LHC the baryon density is small the pressure remains practically constant also at finite baryon densities considered here.
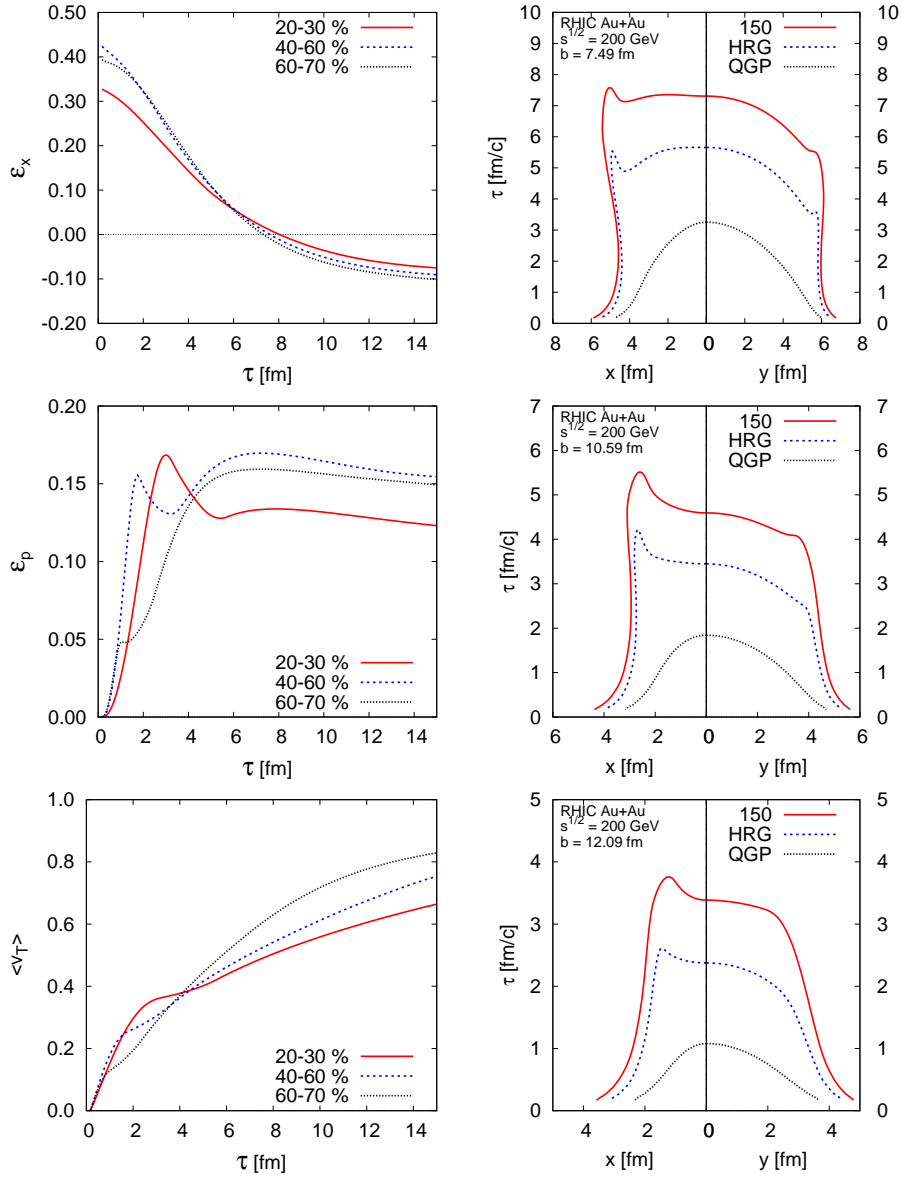
Figure 6.3: The left-hand side shows the time evolution of the spatial eccentricity ε_x, the momentum space eccentricity ε_p and the average transverse velocity $\langle v_T \rangle$ for three different impact parameters in $\sqrt{s_{NN}} = 200$ GeV Au + Au collisions at RHIC. The right-hand side shows the phase boundaries and $T = 150$ MeV isotherms for the same values of the impact parameter as the left-hand side.
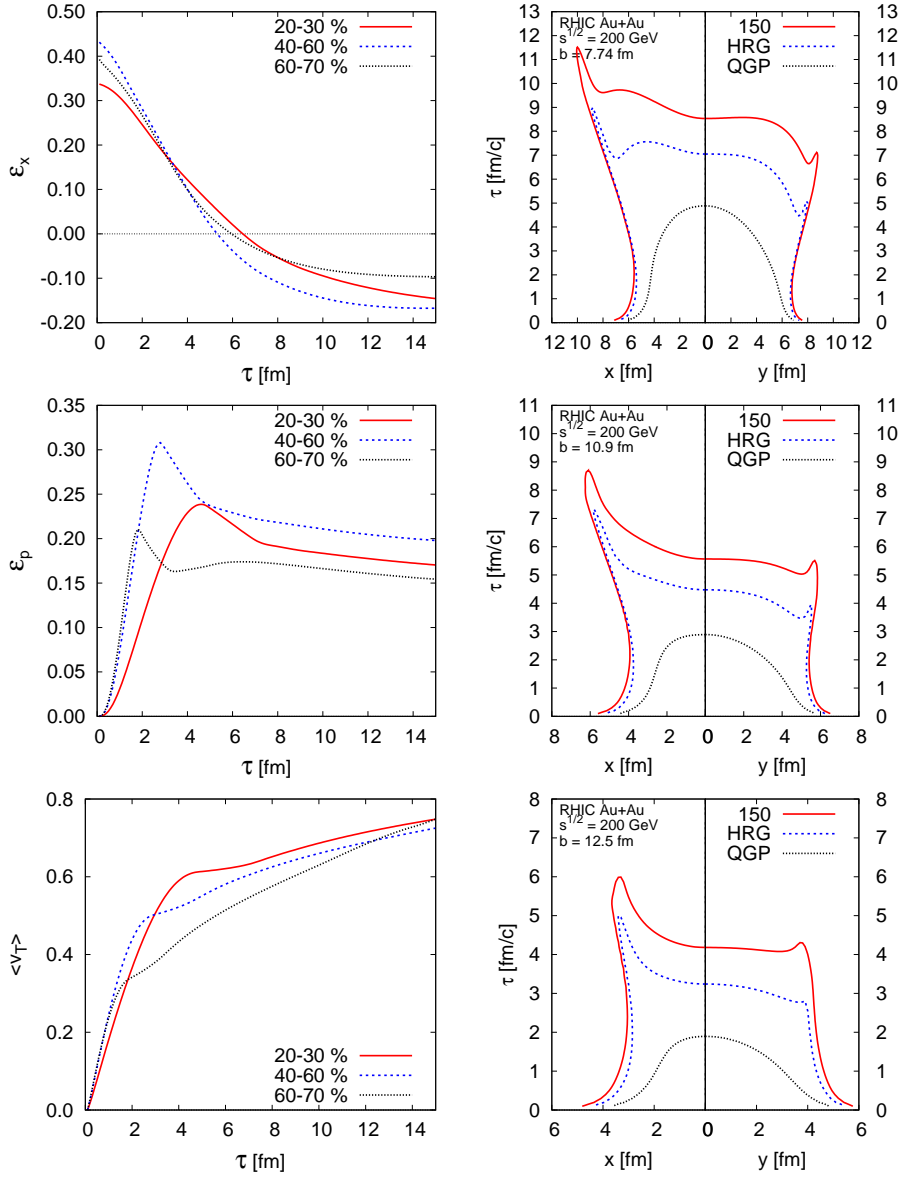
50

Figure 6.4: Same as Fig. 6.3 but for $\sqrt{s_{NN}} = 5500$ GeV Pb + Pb collisions at the LHC. The impact parameters correspond the same centrality classes as in Fig. 6.3, see Table 5.2

.
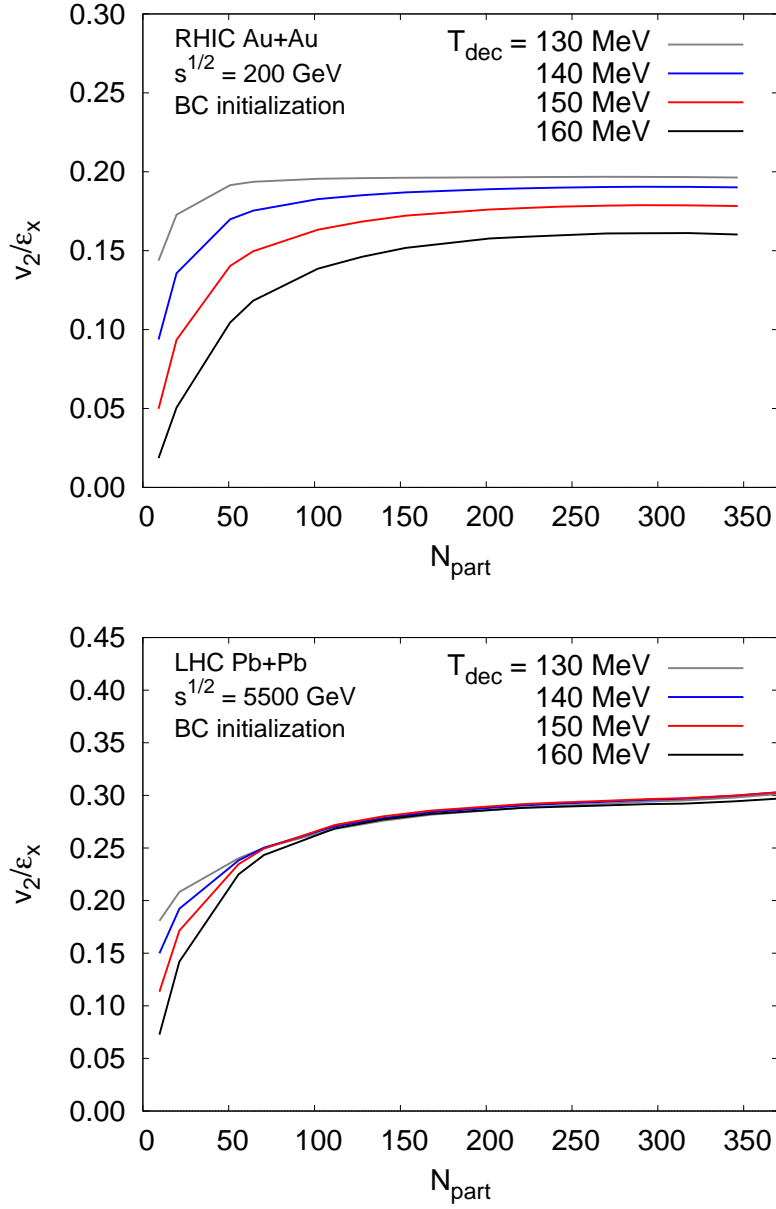
Figure 6.5: The p_T-integrated v_2 for pions divided by the initial spatial eccentricity for the RHIC Au + Au collisions (upper) and for the LHC Pb + Pb collisions (lower) as function of the number of participants. Four different decoupling temperatures are considered.

Chapter 7

Hadron spectra and elliptic flow at RHIC and the LHC

This chapter briefly summarizes the results for the hadron spectra and elliptic flow coefficients obtained from the model and compares them with data for the $\sqrt{s_{NN}} = 200$ GeV Au + Au collisions at RHIC. Also our predictions for the $\sqrt{s_{NN}} = 5500$ GeV Pb + Pb collisions at the LHC are shown. The calculations here include both thermally emitted hadrons and hadrons from the strong and electromagnetic decays of unstable states. The hadron multiplicities and hadron spectra in the most central Au + Au collisions at RHIC at $\sqrt{s_{NN}} = 130$ and 200 GeV are discussed in Refs. [I] and [II]. The predictions for the same observables for the most central collisions at the LHC are given in Ref. [II]. Decoupling conditions at RHIC and the LHC are studied in Ref. [III]. Non-central nuclear collisions, and elliptic flow in particular, are discussed in Ref. [IV] both at RHIC and the LHC.

7.1 Hadron spectra at RHIC

The transverse momentum spectra of pions for different centralities and initializations at RHIC are shown and compared with the PHENIX data [95] in Fig. 7.1. For the eBC initialization the decoupling temperature $T_{\mathrm{dec}} = 150$ MeV and for the eWN initialization $T_{\mathrm{dec}} = 140$ MeV reproduces the data equally well in the low-p_T region. In central and mid-peripheral collisions both initializations give similar results, but the calculations start to separate in more peripheral collisions. This is expected, since the different initializations give a different centrality dependence for the total multiplicity, as was shown in Fig. 5.3. In peripheral collisions, the eBC initial state leads to a much lower multiplicity than the eWN initial state. Similar agreement with the data and calculations is obtained for kaons, as is shown in Fig. 7.2, where the calculations are compared with the PHENIX data [95].

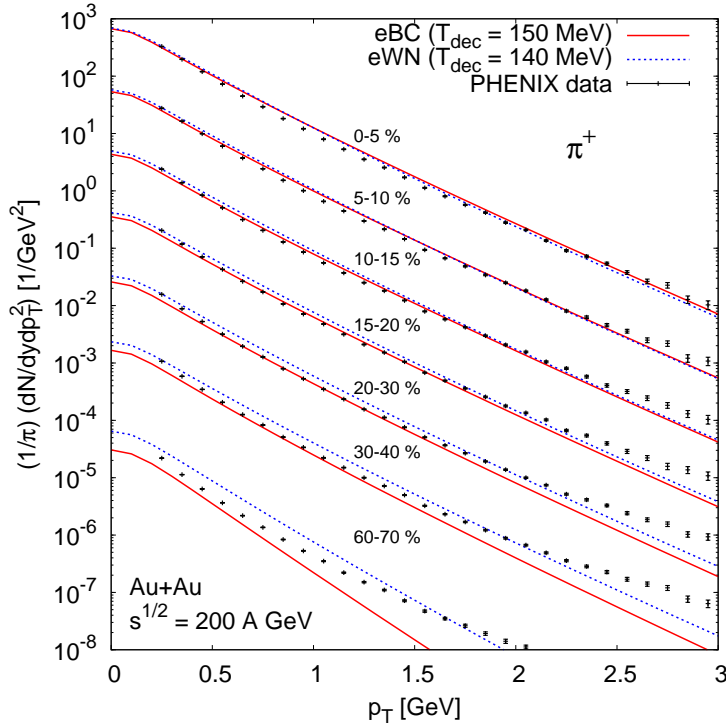The agreement with the data is not as good for protons, as can be seen

Figure 7.1: The p_T spectra of positive pions for $\sqrt{s_{NN}} = 200$ GeV Au + Au collisions at RHIC compared with the PHENIX data [95]. The solid (dashed) lines are for the eBC (eWN) initialization. The centrality classes are indicated in the figure and the spectra are scaled downwards by increasing powers of 10.

in Fig. 7.3 where the calculations are compared with the PHENIX data [95]. With the eBC initialization and $T_{\text{dec}} = 150$ MeV the normalizations of the spectra are quite good, but the p_T slopes are not reproduced. For the eWN initialization also the normalization is below the measured values. A lower decoupling temperature would improve the agreement of the slopes, but the normalization would then fail completely. Also the calculated pion spectra would then overshoot the data. As discussed in the context of the HRG EoS in Chap. 2, the chemical freeze-out is expected to happen before the kinetic freeze-out, leading to the conservation of, e.g. the number of nucleons and anti-nucleons. Also when discussing the dynamical decoupling condition in Chap. 4, it was anticipated that the pions and protons are expected to decouple at different times. Thus it is not necessarily a good approximation to assume the same decoupling condition for all hadron species. These details in the HRG dynamics and decoupling are not, however, considered in this study where we focus on the bulk properties of the strongly interacting matter.
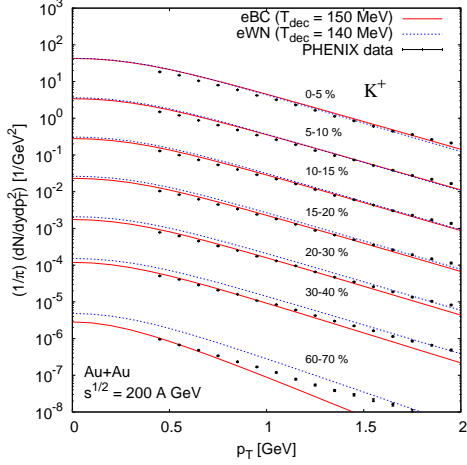
Figure 7.2: Same as Fig. 7.1 but for positive kaons. The data is from the PHENIX Collaboration [95].
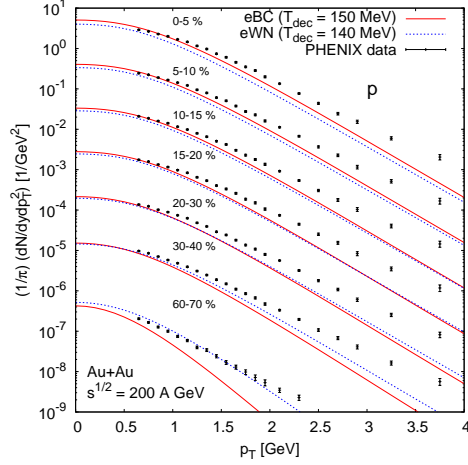
Figure 7.3: Same as Fig. 7.1 but for protons. The data is from the PHENIX Collaboration [95]

7.2 Elliptic flow at RHIC

Figure 7.4 shows the p_T-integrated v_2 of charged hadrons as a function of the number of participants compared with the PHOBOS data [96]. The agreement with the data at $N_{\text{part}} \sim 100 - 300$ is quite good. However, for the most central collisions the model results lie clearly below the data. This is a typical feature in other hydrodynamical models as well, and it is usually associated with the fluctuations in the geometry of the initial state [97], which are expected to have the strongest effect on v_2 in most central collisions. The same behavior can be seen in Fig. 7.5, which shows the differential elliptic flow $v_2(p_T)$ of charged hadrons for different centrality classes with the PHENIX [98] and STAR [99] data. In the most central collision class $v_2(p_T)$ is clearly below the data, while the other centrality classes are fairly well reproduced in the low-p_T region, the data lying well between the results from the two chosen initializations. The difference between the elliptic flow coefficients from the eBC and eWN initializations is quite large. The eBC initialization gives a significantly larger elliptic flow than the eWN initialization for central and mid-peripheral collisions. This is caused by the stronger pressure gradients in the eBC initial state. At very peripheral collisions the situation is reversed. The reason for this is that the lifetime of the QGP in the eBC case drops faster, as a function of increasing impact parameter, than in the eWN case. Therefore, the QGP lifetime is clearly larger with the eWN than with the eBC initial state in the very peripheral collisions, and there is less time for elliptic flow to develop in the eBC case.
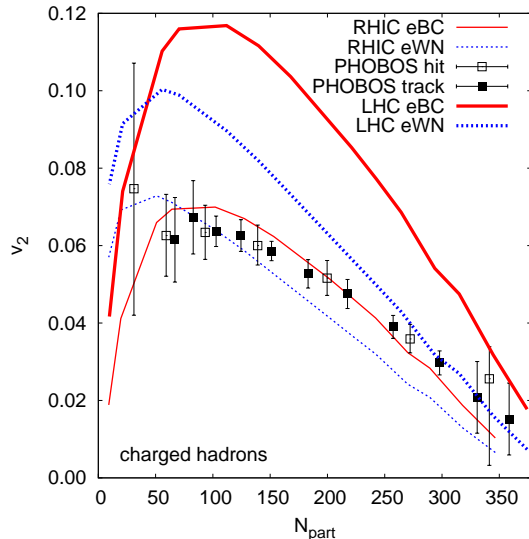
Figure 7.4: The p_T-integrated v_2 of charged hadrons for $\sqrt{s_{NN}} = 200$ GeV Au + Au collisions at RHIC (thin lines) and $\sqrt{s_{NN}} = 5500$ GeV Pb + Pb collisions at the LHC (thick lines) vs. the number of participants. The data is from the PHOBOS collaboration [96]. The statistical and systematic errors are added in quadrature.

The minimum bias $v_2(p_T)$ is defined as [100, 101]

$$v_2^{\text{m.bias}}(y, p_T) \equiv \frac{\int d^2\text{b}\, v_2(y, p_T; b)\frac{dN(b)}{dydp_T^2}}{\int d^2\text{b}\frac{dN(b)}{dydp_T^2}}. \tag{7.1}$$

This is shown for positive pions in Fig. 7.6 together with the PHENIX [98] and STAR [99] data, for positive kaons in Fig. 7.7 with the PHENIX [98] data and for protons in Fig. 7.8 together with the PHENIX [98, 102] and STAR [99] data. For both pions and kaons the RHIC calculations reproduce the data well up to $p_T \sim 1.5$ GeV. Also the uncertainty from the different initializations is smaller in minimum bias $v_2(p_T)$ than for each centrality class separately. Even though, as discussed above, the eBC initialization generates more elliptic flow for central and mid-peripheral collisions than the eWN initial state, the reverse situation for more peripheral collisions leads to partial cancellation when $v_2(p_T)$ is integrated over all centrality classes.

As was the case with the proton p_T spectra, the agreement with the minimum bias $v_2(p_T)$ is not as good for protons, which calls for a more detailed treatment of the HRG dynamics and the freeze-out. A lower decoupling temperature would also improve the agreement with the proton $v_2(p_T)$, but as mentioned before the pion spectra and the number of protons would not be reproduced anymore. We also note that $v_2(p_T)$ for heavier hadrons is be-

low the values for lighter hadrons at fixed p_T, although the p_T-integrated v_2 is larger for heavier hadrons. This can be understood as a result of stronger influence of transverse flow on the p_T of more massive particles [103].
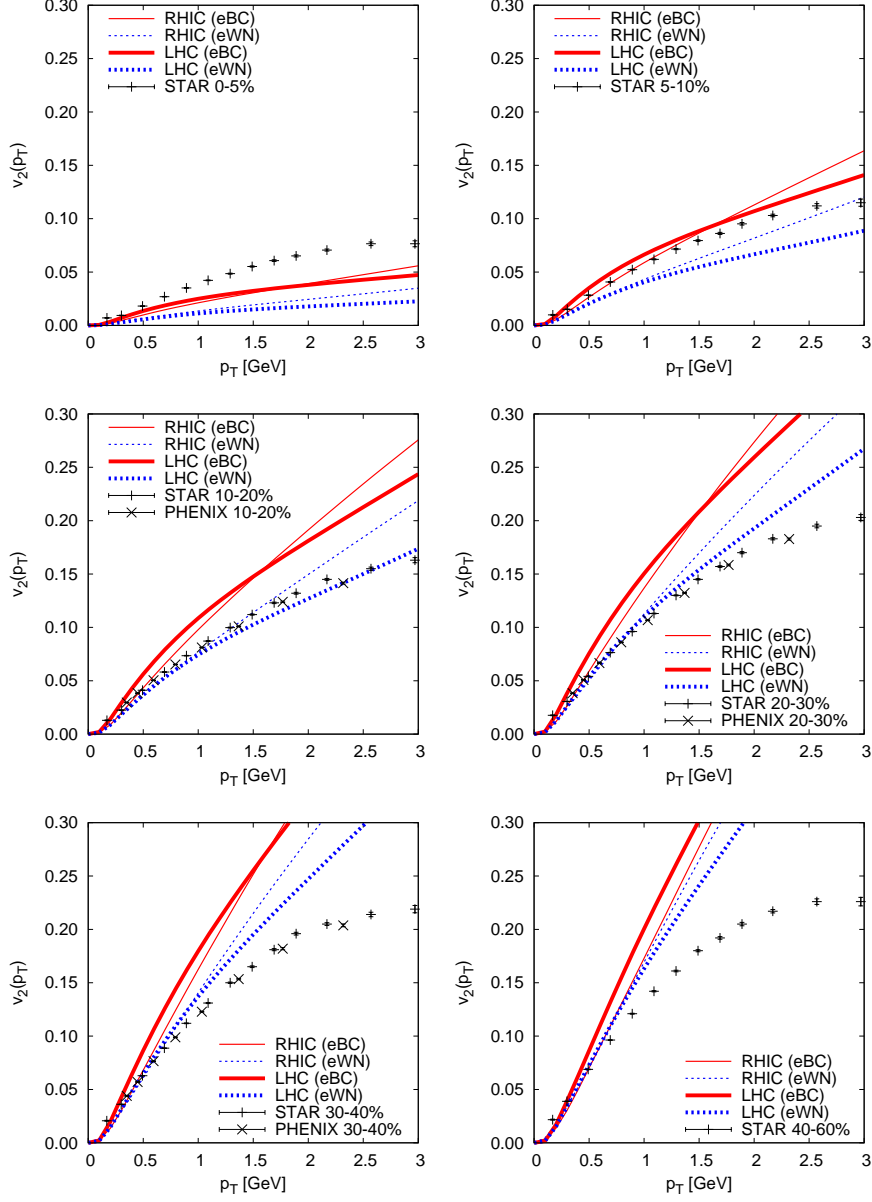

Figure 7.5: The charged hadron $v_2(p_T)$ for different centrality classes for $\sqrt{s_{NN}} = 200$ GeV Au + Au collisions at RHIC (thin lines) and $\sqrt{s_{NN}} = 5500$ GeV Pb + Pb collisions at the LHC (thick lines). The centrality classes are indicated in the figure. The data is from the PHENIX [98] and STAR [99] collaborations.
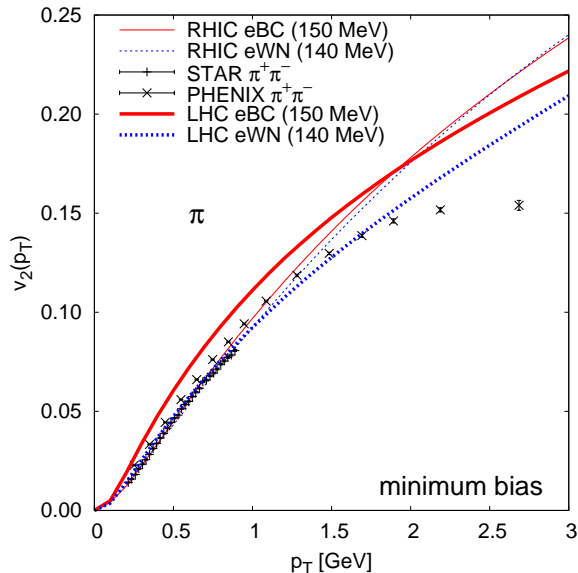
Figure 7.6: The minimum bias $v_2(p_T)$ of pions for $\sqrt{s_{NN}} = 200$ GeV Au + Au collisions at RHIC (thin lines) and $\sqrt{s_{NN}} = 5500$ GeV Pb + Pb collisions at the LHC (thick lines) as a function of transverse momentum. The data is from the PHENIX [98] and STAR [99] collaborations.

7.3 LHC predictions

In spite of the problems with the v_2 results, which are mainly understood, the overall agreement of our model with the RHIC data is quite good for the pion p_T spectra in particular. Thus the model provides a good basis to extend the calculations to the LHC. In the framework presented here, once the EoS is fixed and the EKRT model is used to compute the initial energy and net-baryon densities, essentially the only freedom left is the choice of the decoupling temperature. At RHIC the freeze-out temperature is fixed by comparing the calculated spectra with the data. In the article [III] of this thesis, the dynamical decoupling condition, discussed in Chap. 4, was studied for central collisions. The advantage of this kind of a condition is that it is based on the microscopical scattering rates, and that it depends only on the local conditions of the matter. Therefore, once fixed at one collision system, the decoupling condition is not expected to change between the different systems. Although the freeze-out does not happen at a fixed temperature when the dynamical condition is used [III, 81, 82, 83], it is still possible to find an effective decoupling temperature that on the average describes the decoupling correctly [III]. What we found was that this effective decoupling temperature was essentially unchanged from RHIC to the LHC.

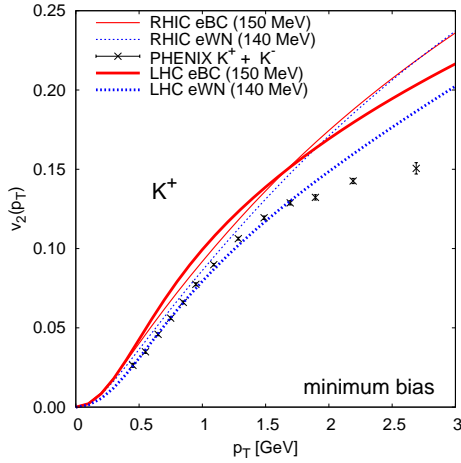Figure 7.9 shows the pion spectra for the same centrality classes as shown

Figure 7.7: As Fig. 7.6 but for kaons. The data is from the PHENIX collaboration [98].
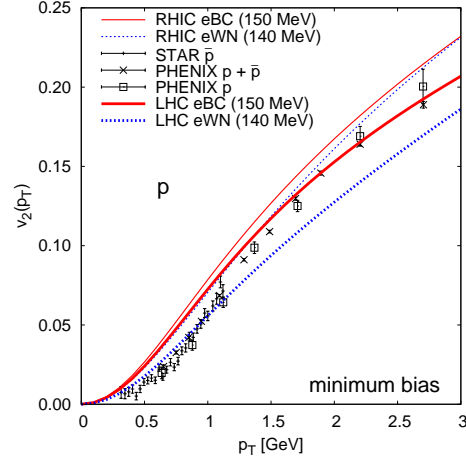
Figure 7.8: The minimum bias $v_2(p_T)$ of protons for $\sqrt{s_{NN}} = 200$ GeV Au + Au collisions at RHIC (thin lines) and $\sqrt{s_{NN}} = 5500$ GeV Pb + Pb collisions at the LHC (thick lines) vs. p_T. The RHIC data are from the STAR [99] and PHENIX [98, 102] collaborations.

in Fig. 7.1, for the LHC initial states discussed in Chap. 5. As the decoupling temperature is not expected to change from RHIC to the LHC, $T_{\text{dec}} = 150$ MeV is used for the eBC initialization and $T_{\text{dec}} = 140$ MeV in the eWN case. As at RHIC also at the LHC both initializations give similar p_T spectra for central and mid-peripheral collisions, but start to differ for more peripheral centrality classes. The larger initial energy density leads to a longer lifetime of the system and therefore also much more transverse flow is generated during the hydrodynamical evolution. This is seen as clearly flatter spectra at the LHC than at RHIC.

The predictions for the p_T-integrated v_2 are shown in Fig. 7.4 together with the RHIC results. The longer lifetime of the QGP phase at the LHC than at RHIC leads also to a larger elliptic flow. The coefficient v_2 is quite sensitive to the chosen initialization already at RHIC, but the sensitivity is even larger at the LHC. However, the lower limit of v_2 predicted by the eWN initialization remains above the RHIC calculations and RHIC data.

The results for the minimum bias $v_2(p_T)$ of pions is shown in Fig. 7.6, for kaons in Fig. 7.7 and for protons in Fig. 7.8. Although the p_T-integrated v_2 is predicted to be clearly above the RHIC results, the situation is not as clear for the p_T-dependent elliptic flow coefficients. For both pions and kaons the upper limit given by the eBC initial state is clearly above the RHIC data and calculations at $p_T \lesssim 2$ GeV, but on the other hand, the lower limits given by the eWN initialization are very close to the RHIC results and even

below them for kaons. The situation remains the same for each centrality class, as seen in Fig. 7.5. The upper limit is clearly above the RHIC results when $p_T \lesssim 1.5$ GeV, but the lower limit goes below them.

Interestingly, for protons both LHC limits are below the RHIC calculations. The model cannot satisfactorily reproduce the proton spectra or the proton elliptic flow at RHIC. However, if the effects not included here go in the same direction at RHIC and the LHC, we would expect from these results that the values of $v_2(p_T)$ at the LHC are below those at RHIC.
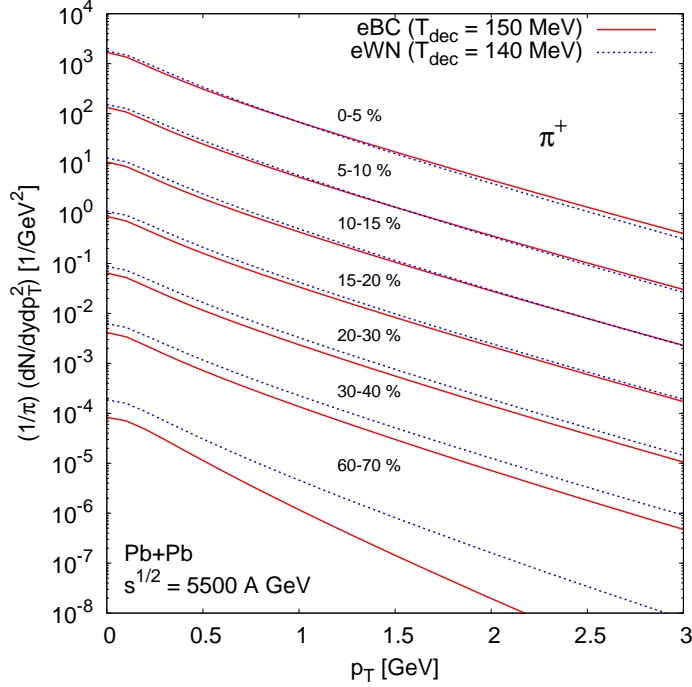

Figure 7.9: The prediction for the p_T spectra of positive pions for $\sqrt{s_{NN}} = 5500$ GeV Pb + Pb collisions at the LHC. The solid (dashed) lines are for the eBC (eWN) initialization. The centrality classes are indicated in the figure and the spectra are scaled downwards by increasing powers of 10.

Finally, it should be emphasized that, as discussed in [II], we expect that the pions from jet fragmentation start to dominate particle production over the hydrodynamical spectra at higher p_T at the LHC than at RHIC. Therefore we predict that the measured p_T spectra and $v_2(p_T)$ should follow the hydrodynamical results higher in p_T at the LHC.

Chapter 8

Conclusions and Outlook

We have studied the space-time evolution of the dense strongly interacting matter formed in central and non-central ultrarelativistic heavy ion collisions at RHIC and at the LHC. The evolution of the particle system was treated using a boost-invariant, relativistic perfect-fluid hydrodynamical model. Hadron spectra from the hydrodynamical solution were calculated using the Cooper-Frye procedure and also the hadron decay contributions were included.

The essential inputs to the hydrodynamical model are the initial energy density, the initial net-baryon density and the EoS. A phenomenological EoS with the HRG phase described as a gas of noninteracting hadrons and hadron resonances and with the QGP phase described by a Bag model EoS of massless quarks and gluons, was used. The QCD phase transition temperature was fixed to $T_c = 165$ MeV, a value consistent with the lattice QCD results. The initial densities for the central nucleus-nucleus collisions were obtained from the EKRT minijet + saturation model [14]. The centrality dependence of the initialization was modeled by using the optical Glauber model.

In [I] the hydrodynamical model was applied for the 5 % most central $\sqrt{s_{NN}} = 130$ GeV Au + Au collisions at RHIC. It was found that a good agreement with the RHIC data is obtained with the decoupling temperature $T_{\mathrm{dec}} = 150$ MeV. The temperature dependence of the slopes of transverse momentum spectra for different EoS's was also studied.

In [II], where an extensive comparison with RHIC data at $\sqrt{s_{NN}} = 130$ GeV and $\sqrt{s_{NN}} = 200$ GeV was carried out, a similar agreement with the RHIC data in the central $\sqrt{s_{NN}} = 200$ GeV Au + Au collisions was found. Also our predictions for the central $\sqrt{s_{NN}} = 5500$ GeV Pb + Pb collisions at the LHC were given in this paper. The initial density profiles used in these studies correspond to the eBC model discussed in this thesis.

In [III] the dynamical decoupling condition was studied and used to constrain the freeze-out condition of pions in central heavy ion collisions at

RHIC and at the LHC. It was concluded that within the approximations used, the effective decoupling temperature remains almost unchanged from RHIC to the LHC. Also the eWN initialization was found to give equal agreement with the eBC initialization when $T_{\text{dec}} = 140$ MeV was used.

In [IV] the hydrodynamical results were generalized to non-central collisions, by the use of the optical Glauber model. The hydrodynamical model was shown to give, at different centralities, a reasonably good description of the hadron p_T spectra and elliptic flow at $\sqrt{s_{NN}} = 200$ GeV Au + Au collisions at RHIC and the corresponding predictions for $\sqrt{s_{NN}} = 5500$ GeV Pb + Pb collisions at the LHC were given. The uncertainties in the extrapolation of the results to the LHC were studied by using both the eWN and eBC initializations. Also the effects of the multiplicity on the elliptic flow coefficients were studied.

The EKRT model is uniquely defined once the proportionality constant c in the saturation condition Eq. (5.8) is fixed in one nucleus-nucleus collision system (one A, one $\sqrt{s_{NN}}$). It can then be used to calculate the initial conditions for any central $A+A$ collision. With the choice $c = 1$ the EKRT + hydrodynamical model correctly predicted the charged hadron multiplicities for central Au + Au collisions at RHIC at $\sqrt{s_{NN}} = 56, 130$ and 200 GeV [33]. The advantage of this closed framework is that it can be straightforwardly extended to the LHC energies.

The uncertainties in the initial transverse distribution of energy density were studied by using the binary collision (eWN) and wounded nucleon (eWN) profiles. Normalization of the wounded nucleon profile was fixed to give the same initial entropy as in the binary profile embedded in the EKRT model. Even though it is straightforward to extend the EKRT model to different energies, this is not the case for an extension to non-central nuclear collisions. Therefore, the centrality dependence was modeled by the optical Glauber model by using the eBC and eWN initializations.

Both initializations give similar transverse momentum spectra for pions and kaons in central and mid-peripheral collisions, provided that the decoupling condition is tuned accordingly. The calculations reproduce the RHIC data in central collisions up to $p_T \sim 2 - 3$ GeV. For more peripheral collisions the agreement with the data does not extend as high in p_T. In mid-peripheral collisions the agreement is reasonably good up to $p_T \sim 1.5$ GeV. The centrality dependence of the eBC and eWN models is different. When fixed to give the same spectra in central collisions, they start to differ towards more peripheral collisions: the eBC model gives systematically smaller hadron multiplicities than the eWN model. The initial conditions at RHIC could be improved, *e.g.* by using a linear combination of the eWN and eBC models such that the centrality dependence at RHIC would be reproduced [13]. However, the coefficients in the linear combination fitted at RHIC could be energy and centrality dependent and would not give a correct centrality dependence at the LHC. For this reason no such fine-tuning of the

initial state is imposed here. Instead, the difference in the two initializations used is taken to represent the uncertainty in the extrapolation from RHIC to the LHC.

As mentioned already above, the agreement between the RHIC data and the calculated p_T spectra of pions and kaons is quite good for $p_T \lesssim 2 - 3$ GeV in central and $p_T \lesssim 1.5$ GeV in peripheral collisions. Also the elliptic flow coefficients are in reasonable agreement with the data for $p_T \lesssim 1.5$ GeV in mid-peripheral collisions. The only place where the data lie clearly outside the limits given by the two initializations is the elliptic flow for the most central collisions, for which the data are above the model prediction. This, however, can be understood to be a result of the fluctuations in the geometry of the initial state [97], which are not included in our model.

For the most peripheral nuclear collisions considered the p_T spectra of pions and kaons are still well within the uncertainty limits. However, the difference between the limits also grows quite large in these collisions. While the p_T-integrated v_2 is still well reproduced, the differential $v_2(p_T)$ starts to deviate from the data already at quite low p_T values. It is clear that the hydrodynamical modeling cannot be expected to work for very small systems, thus it is not suprising to see the deviations from the hydrodynamical behavior in very peripheral nuclear collisions.

Although the transverse momentum spectra and elliptic flow of pions and kaons are quite well reproduced at RHIC, the same is not true for protons. The normalization of the computed proton spectra is quite good with the eBC initialization, with $T_{\rm dec} = 150$ MeV, but the eWN initialization, with $T_{\rm dec} = 140$ MeV, gives too few protons. The slopes of the proton spectra are not given correctly by either one of the initial states. Also too large $v_2(p_T)$ values are obtained. This could perhaps be improved by using a more detailed model for the HRG dynamics and for the decoupling of hadrons.

The uncertainty in the transverse momentum spectra, originating from the initial transverse profiles is very similar at the LHC as at RHIC. The p_T-integrated v_2 is predicted to be clearly larger at the LHC than at RHIC, but also the uncertainty from the initial transverse profiles is larger. This is due to the longer lifetime of the QGP at the LHC: not only the elliptic flow, but also the difference between the elliptic flow resulting from the two initializations has more time to grow. In contrast, the effects of the HRG dynamics to the integrated v_2 are anticipated to be smaller at the LHC, since the azimuthal anisotropy of the pressure gradients have almost vanished in the HRG at the LHC. The differential $v_2(p_T)$ is not expected to change very much from RHIC to the LHC, but still it is found to be more sensitive to the initial state at the LHC. The same is true for the minimum bias $v_2(p_T)$ and for each centrality class separately. Also the effects of the multiplicity on the elliptic flow were studied in Ref. [IV]. It was found that the p_T-integrated v_2 is quite sensitive to the multiplicity, but $v_2(p_T)$ has a much weaker dependence.

In general a good simultaneous agreement of the low-p_T pion and proton observables can be obtained with the hybrid models [65, 66, 67, 68, 69]. In these models the QGP is described by hydrodynamical models, but the HRG is described by microscopical hadron cascade models. It would be interesting to see whether the full microscopic treatment of the HRG dynamics is necessary, or could a similar agreement with the data be obtained from the hydrodynamical modeling alone by considering separate chemical decoupling, and different dynamical kinetic freeze-out conditions for different hadron species. In the future also an improved EoS should be considered, by using the lattice QCD and lattice QCD inspired results for the QGP, instead of the simplified Bag model version with a first order phase transition. In addition to the non-equilibrium effects in the HRG, also the viscosity in the QGP phase is expected to play a role in a detailed understanding of the whole time-evolution of the strongly interacting system.

There are other effects which need to be included in hydrodynamical models for more detailed description of the p_T spectra. In addition to the non-equilibrium effects mentioned above, in the transition region from the hydrodynamic to pQCD regime, coalescence models [104, 105] should be combined with hydrodynamics. However, for the bulk of produced particles, the low-p_T pions and kaons, the full equilibrium model is in a good enough agreement with the RHIC data to give confidence to make baseline, full equilibrium, predictions for the same observables at the LHC.

Bibliography

[I]   K. J. Eskola, H. Niemi, P. V. Ruuskanen and S. S. Räsänen, Phys. Lett. B **566**, 187 (2003) [arXiv:hep-ph/0206230].

[II] K. J. Eskola, H. Honkanen, H. Niemi, P. V. Ruuskanen and S. S. Räsänen, Phys. Rev. C **72**, 044904 (2005) [arXiv:hep-ph/0506049].

[III] K. J. Eskola, H. Niemi and P. V. Ruuskanen, Phys. Rev. C **77**, 044907 (2008) [arXiv:0710.4476 [hep-ph]].

[IV] H. Niemi, K. J. Eskola and P. V. Ruuskanen, arXiv:0806.1116 [hep-ph], submitted to Phys. Rev. C.

[1] W. M. Yao *et al.* [Particle Data Group], J. Phys. G **33**, 1 (2006).

[2] J. C. Collins and M. J. Perry, Phys. Rev. Lett. **34**, 1353 (1975).

[3] F. Karsch, PoS **LATTICE2007**, 015 (2007) [arXiv:0711.0661 [hep-lat]].

[4] Quark Matter' 06 Proceedings, edited by Y. G. Ma, E. K. Wang, X. Cai, H. Z. Huang, X. N. Wang, Z. Y. Zhu, J. Phys. G **34**, S173 (2007)

[5] CERN Press Release 10.02.2008.

[6] D. Molnar and M. Gyulassy, Phys. Rev. C **62**, 054907 (2000) [arXiv:nucl-th/0005051].

[7] Z. Xu and C. Greiner, Phys. Rev. C **71**, 064901 (2005) [arXiv:hep-ph/0406278].

[8] L. D. Landau, Izv. Akad. Nauk Ser. Fiz. **17**, 51 (1953).

[9] J. D. Bjorken, Phys. Rev. D **27**, 140 (1983).

[10] K. Kajantie and L. D. McLerran, Phys. Lett. B **119**, 203 (1982); Nucl. Phys. B **214**, 261 (1983).

[11] K. Kajantie and R. Raitio, Phys. Lett. B **121**, 415 (1983); K. Kajantie, R. Raitio and P. V. Ruuskanen, Nucl. Phys. B **222**, 152 (1983).

[12] J. Sollfrank, P. Huovinen, M. Kataja, P. V. Ruuskanen, M. Prakash and R. Venugopalan, Phys. Rev. C **55**, 392 (1997) [arXiv:nucl-th/9607029].

[13] P. F. Kolb, U. W. Heinz, P. Huovinen, K. J. Eskola and K. Tuominen, Nucl. Phys. A **696**, 197 (2001) [arXiv:hep-ph/0103234].

[14] K. J. Eskola, K. Kajantie, P. V. Ruuskanen and K. Tuominen, Nucl. Phys. B **570**, 379 (2000) [arXiv:hep-ph/9909456].

[15] E. Iancu and R. Venugopalan, in Quark-Gluon Plasma 3, edited by R. C. Hwa and X. N. Wang, (World Scientific, Singapore, 2004), arXiv:hep-ph/0303204.

[16] I. Arsene *et al.* [BRAHMS Collaboration], Nucl. Phys. A **757**, 1 (2005) [arXiv:nucl-ex/0410020].

[17] B. B. Back *et al.*, Nucl. Phys. A **757**, 28 (2005) [arXiv:nucl-ex/0410022].

[18] K. Adcox *et al.* [PHENIX Collaboration], Nucl. Phys. A **757**, 184 (2005) [arXiv:nucl-ex/0410003].

[19] J. Adams *et al.* [STAR Collaboration], Nucl. Phys. A **757**, 102 (2005) [arXiv:nucl-ex/0501009].

[20] P. Huovinen, in Quark-Gluon Plasma 3, edited by R. C. Hwa and X. N. Wang, (World Scientific, Singapore, 2004), arXiv:nucl-th/0305064.

[21] P. Kolb and U. W. Heinz, in Quark-Gluon Plasma 3, edited by R. C. Hwa and X. N. Wang, (World Scientific, Singapore, 2004), arXiv:nucl-th/0305084.

[22] P. Huovinen and P. V. Ruuskanen, Ann. Rev. Nucl. Part. Sci. **56**, 163 (2006) [arXiv:nucl-th/0605008].

[23] P. F. Kolb, J. Sollfrank and U. W. Heinz, Phys. Rev. C **62**, 054909 (2000) [arXiv:hep-ph/0006129].

[24] M. Gyulassy and L. McLerran, Nucl. Phys. A **750**, 30 (2005) [arXiv:nucl-th/0405013].

[25] P. Danielewicz and M. Gyulassy, Phys. Rev. D **31**, 53 (1985).

[26] D. Teaney, Phys. Rev. C **68**, 034913 (2003) [arXiv:nucl-th/0301099].

[27] A. Muronga and D. H. Rischke, arXiv:nucl-th/0407114.

[28] P. Romatschke and U. Romatschke, Phys. Rev. Lett. **99**, 172301 (2007) [arXiv:0706.1522 [nucl-th]].

[29] H. Song and U. W. Heinz, Phys. Rev. C **77**, 064901 (2008) [arXiv:0712.3715 [nucl-th]].

[30] M. Luzum and P. Romatschke, arXiv:0804.4015 [nucl-th].

[31] K. Dusling and D. Teaney, Phys. Rev. C **77**, 034905 (2008) [arXiv:0710.5932 [nucl-th]].

[32] A. K. Chaudhuri, arXiv:0801.3180 [nucl-th].

[33] K. J. Eskola, P. V. Ruuskanen, S. S. Rasanen and K. Tuominen, Nucl. Phys. A **696**, 715 (2001) [arXiv:hep-ph/0104010].

[34] K. J. Eskola, H. Niemi and P. V. Ruuskanen, arXiv:0705.2114 [hep-ph].

[35] K. J. Eskola, H. Honkanen, H. Niemi, P. V. Ruuskanen and S. S. Räsänen, arXiv:0705.1770 [hep-ph].

[36] T. Hirano, Prog. Theor. Phys. Suppl. **168**, 347 (2007) [arXiv:0704.1699 [nucl-th]].

[37] M. Bluhm, B. Kampfer, R. Schulze, D. Seipt and U. Heinz, Phys. Rev. C **76**, 034901 (2007) [arXiv:0705.0397 [hep-ph]].

[38] M. Chojnacki, W. Florkowski, W. Broniowski and A. Kisiel, arXiv:0712.0947 [nucl-th].

[39] A. K. Chaudhuri, arXiv:0803.0643 [nucl-th].

[40] N. Armesto *et al.*, J. Phys. G **35**, 054001 (2008) [arXiv:0711.0974 [hep-ph]].

[41] N. Armesto, arXiv:0804.4158 [hep-ph].

[42] S. A. Bass *et al.*, Prog. Part. Nucl. Phys. **41**, 255 (1998) [arXiv:nucl-th/9803035].

[43] L.D. Landau and E.M. Lifshitz, Fluid mechanics (Pergamon, New York, 1959)

[44] D. H. Rischke, [arXiv:nucl-th/9809044].

[45] S.R. deGroot, W.A. van Leeuwen and Ch.G. van Weert, Relativistic Kinetic Theory (North-Holland, Amsterdam, 1980)

[46] I. Müller, Z. Phys. **198**, 329 (1967).

[47] W. Israel, Annals Phys. **100**, 310 (1976).

[48] J.M. Stewart, Proc. Roy. Soc. **A 357**, 59 (1977).

[49] W. Israel and J. M. Stewart, Annals Phys. **118**, 341 (1979).

[50] T. Hirano, Phys. Rev. C **65**, 011901 (2002) [arXiv:nucl-th/0108004].

[51] K. J. Eskola, K. Kajantie and P. V. Ruuskanen, Eur. Phys. J. C **1**, 627 (1998) [arXiv:nucl-th/9705015].

[52] T. Hirano, K. Morita, S. Muroya and C. Nonaka, Phys. Rev. C **65**, 061902 (2002) [arXiv:nucl-th/0110009].

[53] H. Von Gersdorff, L. D. McLerran, M. Kataja and P. V. Ruuskanen, Phys. Rev. D **34**, 794 (1986).

[54] P. V. Ruuskanen, Acta Phys. Polon. B **18**, 551 (1987).

[55] A. Chodos, R. L. Jaffe, K. Johnson, C. B. Thorn and V. F. Weisskopf, Phys. Rev. D **9**, 3471 (1974).

[56] D. E. Groom *et al.* [Particle Data Group], Eur. Phys. J. C **15**, 1 (2000).

[57] R. Venugopalan and M. Prakash, Nucl. Phys. A **546**, 718 (1992).

[58] F. Karsch, K. Redlich and A. Tawfik, Eur. Phys. J. C **29**, 549 (2003) [arXiv:hep-ph/0303108].

[59] R. Stock, Nucl. Phys. A **661**, 282 (1999) [arXiv:hep-ph/9911408].

[60] R. Rapp, Phys. Rev. C **66**, 017901 (2002) [arXiv:hep-ph/0204131].

[61] T. Hirano and K. Tsuda, Phys. Rev. C **66**, 054905 (2002) [arXiv:nucl-th/0205043].

[62] P. F. Kolb and R. Rapp, Phys. Rev. C **67**, 044903 (2003) [arXiv:hep-ph/0210222].

[63] P. Huovinen, arXiv:0710.4379 [nucl-th].

[64] P. Huovinen and J. I. Kapusta, Phys. Rev. C **69**, 014902 (2004) [arXiv:nucl-th/0310051].

[65] S. A. Bass and A. Dumitru, Phys. Rev. C **61**, 064909 (2000) [arXiv:nucl-th/0001033].

[66] D. Teaney, J. Lauret and E. V. Shuryak, arXiv:nucl-th/0110037.

[67] T. Hirano, U. W. Heinz, D. Kharzeev, R. Lacey and Y. Nara, Phys. Rev. C **77**, 044909 (2008) [arXiv:0710.5795 [nucl-th]].

[68] T. Hirano, U. W. Heinz, D. Kharzeev, R. Lacey and Y. Nara, Phys. Lett. B **636**, 299 (2006) [arXiv:nucl-th/0511046].

[69] C. Nonaka and S. A. Bass, Phys. Rev. C **75**, 014902 (2007) [arXiv:nucl-th/0607018].

[70] M. Laine and Y. Schroder, Phys. Rev. D **73**, 085009 (2006) [arXiv:hep-ph/0603048].

[71] P. Huovinen, Nucl. Phys. A **761**, 296 (2005) [arXiv:nucl-th/0505036].

[72] J. Randrup, Phys. Rev. Lett. **92**, 122301 (2004) [arXiv:hep-ph/0308271].

[73] J.P. Boris and D.L. Book, J. Comp. Phys. **11**, 38 (1973); D.L. Book, J.P. Boris and K. Hain, J. Comp. Phys. **18**, 248 (1975).

[74] S.T. Zalesak, J. Comp. Phys. **31**, 335 (1979).

[75] D. H. Rischke, S. Bernard and J. A. Maruhn, Nucl. Phys. A **595**, 346 (1995) [arXiv:nucl-th/9504018].

[76] D. H. Rischke, Y. Pursun and J. A. Maruhn, Nucl. Phys. A **595**, 383 (1995) [Erratum-ibid. A **596**, 717 (1996)] [arXiv:nucl-th/9504021].

[77] P. Huovinen, M.Sc. thesis, Department of Physics, University of Jyväskylä, 1996.

[78] P. Huovinen, PhD thesis, Department of Physics, University of Jyväskylä, 1999.

[79] J. P. Bondorf, S. I. A. Garpman and J. Zimanyi, Nucl. Phys. A **296**, 320 (1978).

[80] U. Mayer and U. W. Heinz, Phys. Rev. C **56**, 439 (1997).

[81] C. M. Hung and E. V. Shuryak, Phys. Rev. C **57**, 1891 (1998) [arXiv:hep-ph/9709264].

[82] A. Dumitru, Phys. Lett. B **463**, 138 (1999) [arXiv:hep-ph/9905217].

[83] U. Heinz and G. Kestin, PoS **CPOD2006**, 038 (2006) [arXiv:nucl-th/0612105].

[84] U. W. Heinz and G. Kestin, arXiv:0709.3366 [nucl-th].

[85] F. Cooper and G. Frye, Phys. Rev. D **10**, 186 (1974).

[86] J. Sollfrank, P. Koch and U. W. Heinz, Z. Phys. C **52**, 593 (1991).

[87] S. S. Räsänen, M.Sc. thesis, Department of Physics, University of Jyväskylä, 2001.

[88] G. Bertsch, M. Gong, L. D. McLerran, P. V. Ruuskanen and E. Sarkki-nen, Phys. Rev. D **37**, 1202 (1988).

[89] R. Vogt, Acta Phys. Hung. New Ser. Heavy Ion Phys. **9**, 339 (1999) [arXiv:nucl-th/9903051].

[90] D. d'Enterria, [arXiv:nucl-ex/0302016].

[91] K. J. Eskola, K. Kajantie and K. Tuominen, Phys. Lett. B **497**, 39 (2001) [arXiv:hep-ph/0009246].

[92] K. J. Eskola, K. Kajantie and K. Tuominen, Nucl. Phys. A **700**, 509 (2002) [arXiv:hep-ph/0106330].

[93] S. Voloshin and Y. Zhang, Z. Phys. C **70**, 665 (1996) [arXiv:hep-ph/9407282].

[94] J. Y. Ollitrault, Phys. Rev. D **46**, 229 (1992).

[95] S. S. Adler *et al.* [PHENIX Collaboration], Phys. Rev. C **69**, 034909 (2004) [arXiv:nucl-ex/0307022].

[96] B. B. Back *et al.* [PHOBOS Collaboration], Phys. Rev. C **72**, 051901 (2005) [arXiv:nucl-ex/0407012].

[97] M. Miller and R. Snellings, arXiv:nucl-ex/0312008.

[98] A. Adare *et al.* [PHENIX Collaboration], Phys. Rev. Lett. **98**, 162301 (2007) [arXiv:nucl-ex/0608033].

[99] J. Adams *et al.* [STAR Collaboration], Phys. Rev. C **72**, 014904 (2005) [arXiv:nucl-ex/0409033].

[100] K. H. Ackermann *et al.* [STAR Collaboration], Phys. Rev. Lett. **86**, 402 (2001) [arXiv:nucl-ex/0009011].

[101] P. F. Kolb, P. Huovinen, U. W. Heinz and H. Heiselberg, Phys. Lett. B **500**, 232 (2001) [arXiv:hep-ph/0012137].

[102] S. S. Adler *et al.* [PHENIX Collaboration], Phys. Rev. Lett. **91**, 182301 (2003) [arXiv:nucl-ex/0305013].

[103] P. Huovinen, P. F. Kolb, U. W. Heinz, P. V. Ruuskanen and S. A. Voloshin, Phys. Lett. B **503**, 58 (2001) [arXiv:hep-ph/0101136].

[104] R. J. Fries, B. Muller, C. Nonaka and S. A. Bass, Phys. Rev. C **68**, 044902 (2003) [arXiv:nucl-th/0306027].

[105] R. C. Hwa, arXiv:0804.3763 [nucl-th].